JOURNAL OF AIRCRAFT
Vol. 44, No. 6, November–December 2007

Forebody Geometry Effects on the Flowfield of a Blunt-Nose Projectile at High Alpha

Javier Lopera* and T. Terry Ng†
University of Toledo, Toledo, Ohio 43606
and
Mehul P. Patel‡ and Russ Stucke§
Orbital Research, Inc., Cleveland, Ohio 44103

DOI: 10.2514/1.31783

Wind-tunnel experiments are conducted on a projectile at high incidence to examine the effect of nose shapes and a passive strake control device on the side force and yawing moment. The study was also aimed at gaining some insights into the fluid mechanics of blunt-nose bodies of revolution at high angles of attack. Detailed flow visualization and force measurements are obtained on a projectile with a fineness ratio of 4 at a Reynolds number of 0.19×10^6 and 42- and 48-deg angles of attack. Off- and on-surface flow visualization records are collected to study the effects of two blunt noses: a hemispherical nose and an elliptical nose with 33% ellipticity. It was found that the elliptical nose results in flow behaviors typical of a blunt nose, whereas the hemispheric nose results in behaviors that are akin to a pointed nose. An explanation for the contrasting behaviors is provided.

Nomenclature

C_M	=	pitching-moment coefficient
C_n	=	yawing-moment coefficient
C_Y	=	side-force coefficient
D	=	maximum diameter of body of revolution
e	=	ellipticity of forebody
h_{strake}	=	deployment height of aftbody strake
L	=	body length
L_{rb}	=	length of recirculation bubble
L_{strake}	=	length of aftbody strake
M	=	freestream Mach number
Re	=	Reynolds number based on D and U
U	=	freestream velocity
x	=	distance from nose apex
α	=	angle of attack, deg
α_{AV}	=	onset angle of attack of asymmetric vortices, deg
α_{SV}	=	onset angle of attack of symmetric vortices, deg
α_{UV}	=	onset angle of attack of unsteady vortices, deg
β	=	sideslip angle, deg
θ	=	azimuthal strake location relative to windward meridian, pilot's view, deg
θ_A	=	forebody apex half-angle, deg

I. Introduction

THE design and operation of current missiles, projectiles, and aircraft often requires them to operate and perform maneuvers at high angles of attack. It has been long recognized that at high angles of attack, slender bodies encounter separation and vortex-induced yaw caused by asymmetric vortex shedding even at $\beta = 0$ deg. These large side forces generate large phantom yawing moments and are of a great concern, because their induced yawing moments can be an order of magnitude larger than the available control obtained from full rudder deflection [1]. Over the years, extensive research has been conducted for the control of forebody flow asymmetries at high incidence using different types of forebody control devices, and results have shown that a projectile's maneuvering performance can be greatly enhanced through proper exploitation of these forces.

Slender bodies of revolution advance through four distinct flow regimes when they are pitched from 0 to 90 deg, in which each subsequent flow regime reflects the diminishing influence of the axial-flow component [1]. Figure 1, reproduced from [1], illustrates the effect of angle of attack on the leeside flowfield. The axial-flow component dominates at low angles of attack ($0 \leq \alpha \leq \alpha_{\text{SV}}$) and the flow is attached, whereas crossflow effects cause a thickening of the boundary layer on the leeside. It is important to mention that if the nose is blunt, the so-called nose-induced separation of the axial flow will take place as described by Ericsson and Reding [2]. This closed-type flow separation, which is often associated with standing, tornadolike, vortices [3], creates reattaching flow on the aftbody, which subsequently delays the development of open-type flow separation on the aftbody with accompanying body vortices [4]. For intermediate angles of attack ($\alpha_{\text{SV}} \leq \alpha \leq \alpha_{\text{AV}}$), the crossflow separates and rolls up into a symmetric vortex pair. At higher angles of attack ($\alpha_{\text{AV}} \leq \alpha \leq \alpha_{\text{UV}}$), asymmetric flow separation occurs and a side force and yawing moment are generated at zero sideslip. At very high angles of attack ($\alpha_{\text{UV}} \leq \alpha \leq 90$ deg), the axial component is greatly diminished and flow separation and vortex shedding become unsteady, starting on the aftbody and advancing toward the nose with increasing angle of attack. At this very high angle of attack, the leeside flow resembles the wake of a two-dimensional cylinder normal to the flow.

Another fundamental phenomenon over slender bodies is that there are two different types of steady asymmetric vortex shedding. The first type occurs on pointed bodies in which the vortex asymmetry, and thus the side force, tends to commence at the nose. With this type of vortex shedding, vortices are shed at a relatively fast rate to give alternating side-force cells on long slender bodies [5,6]. The second type of vortex shedding occurs when a slight amount of nose bluntness, sometimes as little as 6%, is applied to the nose. In this vortex shedding regime, asymmetric vortices develop initially at the rear of the body, and the alternating vortex shedding does not occur as readily. This implies that large side-force cells can cover the entire cylindrical aftbody.

Presented as Paper 461 at the 45th AIAA Aerospace Sciences Meeting and Exhibit, Reno, NV, 8–11 January 2007; received 24 April 2007; revision received 6 July 2007; accepted for publication 10 July 2007.

*Graduate Research Assistant, Department of Mechanical, Industrial and Manufacturing Engineering. Member AIAA.
†Professor, Department of Mechanical, Industrial and Manufacturing Engineering. Senior Member AIAA.
‡Director, Aerodynamics Group. Senior Member AIAA.
§Aerospace Engineer. Member AIAA.

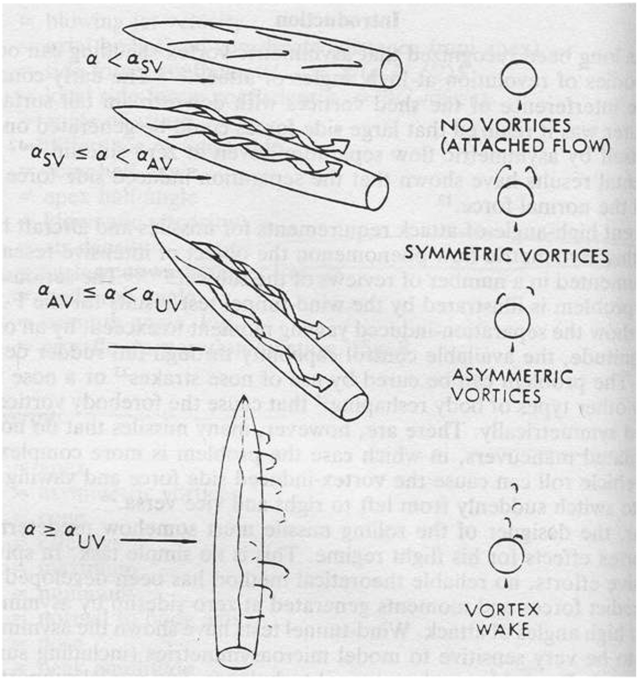

Fig. 1 Effect of angle of attack on leeside flowfield (reproduced from [1]).

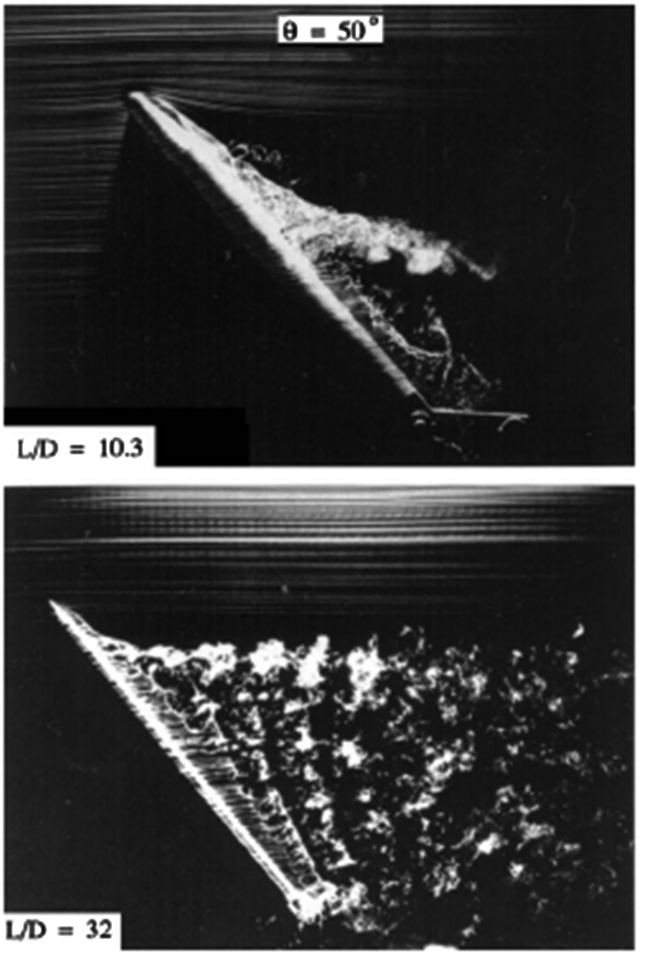

Fig. 2 Effect of aspect ratio on the flow regime at $\alpha = 50$ deg (reproduced from [8]).

Some researchers have shown that asymmetric vortices generated by a slender forebody are not affected by the aftbody vortices initially. Keener et al. [7] demonstrated this premise, showing that the cylindrical aftbody has no effect on the side force generated on the pointed ogive nose. In contrast, Montividas et al. [8] showed that the aspect ratio of a slender body has a significant effect on the flow regime developed at high angles of attack. Figure 2, reproduced from [8], shows visualizations at $\alpha = 50$ deg for a slender body with an aspect ratio $L/D = 10.3$ and 32. The smaller aspect ratio showed a flow pattern with an asymmetric separation of a steady longitudinal vortex, whereas the larger aspect ratio produced a flowfield that included asymmetric separation of tip vortices, an unsteady flow regime, and vortex shedding on the aftbody.

The present work is aimed at gaining insight into the effect of nose geometry on the baseline flowfield and control of vortices at high incidence on a short blunt-nose projectile. The projectile examined is part of a novel countermeasure defense concept designated as destructive expendable (DEX) [9–15]. Detailed off- and on- surface flow visualizations will be presented, in addition to force measurements. A vast amount of research in the field of high-alpha control, asymmetric flow control, and side-force alleviation can be found in the literature for pointed and ogive bodies, but a relatively small field of research has been conducted on short blunt bodies, such as the model discussed herein.

II. Background

In 1951, Allen and Perkins [16] were the first researchers to note the presence of asymmetric vortex flow behind an axisymmetric body at high angles of attack. Allen and Perkins [17] introduced a breakthrough paper discussing the use of an "impulsive cross-flow analogy" to allow for viscous effects on the force and moment characteristics of bodies of revolution that is still the basis for modern aerodynamic prediction tools for slender bodies. Peake et al. [18] discussed that vortex asymmetry was initially influenced by conditions at the pointed nose and Mach number, and once it started it was influenced by the afterbody length. They also indicated that increasing the Reynolds number seemed to delay the onset of asymmetry.

Lamont and Hunt [19] conducted detailed investigations of the pressure and force distribution of bodies of revolution at high incidence and found large out-of-plane forces. They also showed that the measured value of side forces and level of unsteadiness can vary with roll angle. Rao [20] had early success in suppressing side forces at high incidence by mounting a pair of helical trips on pointed forebodies. Ericsson and Reding [21,22] assessed that small nose bluntness, nose booms, nose strakes, or body trips could be used effectively on a pointed slender body to reduce vortex-induced asymmetric loads. Later, Ericsson and Reding [23] pointed out the detrimental and dangerous effects that a coupling of the vehicle motion and asymmetric vortex shedding could have on the rigid and elastic response of long slender bodies.

Brandon and Nguyen [24] conducted experiments on a generic airplane model and showed that forebody cross-sectional shape and fineness ratio, among other factors, can strongly affect both static and dynamic (roll) stability at high incidence. In the same year, Ericsson [25] presented a breakthrough paper on the moving wall effects on boundary-layer transition and separation that added to the understanding of high-alpha unsteady flows. Ward and Katz [26] conducted flow visualization experiments on an inclined ogive nose cone and demonstrated that the lee structure was asymmetric throughout the model and was dominated by continuously generated, multiple, large-scale flow structures. Degani and Schiff [27] and Degani [28] were the first to successfully numerically simulate the marked asymmetry that occurred experimentally on slender bodies of revolution at high angles of attack. Zilliac et al. [29] studied an inclined ogive cylinder and concluded that microvariations in the tip geometry have a large influence on the downstream development of the flowfield. Luo et al. [30] examined a sharp-nose ogive cylinder and an elliptic-tip ogive cylinder and showed that the elliptic tip produced more predictable side forces with different roll angles than the sharp ogive tip. Lua et al. [31] used circular trips and helical grooves on a tangent ogive nose cylinder and discovered that the circular trips were more effective in reducing side forces at high angles of attack.

Hsieh [3] conducted early supersonic investigations on the flow over a hemisphere cylinder at incidence and showed that two separation regions, the nose separation bubble and the crossflow separation zone, could exist simultaneously at intermediate incidence. Later, Hsieh and Wang [32] used thin-layer Navier–Stokes solutions to simulate incompressible laminar flow over a hemisphere cylinder at incidence. Numerical simulations were conducted by assuming a symmetrical flow with respect to the pitching plane. Results showed complex separated flow structures, particularly close to the nose, and a number of intricate structural characteristics unique to three-dimensional flows. Hoang et al. [33] investigated a hemisphere cylinder at low Reynolds numbers and incidences up to $\alpha = 45$ deg. They documented the appearance of nose vortex rings and horn vortices, and they observed a symmetric flowfield. Further studies were conducted by Hoang et al. [34] on a hemisphere cylinder at incidences up to $\alpha = 30$ deg for intermediate to high Reynolds numbers. They found that at low incidences the separation bubble takes the form of a ring, but as the incidence increases it becomes an isolated bubble. The authors discussed that the nose structures are not connected with the separation lines that give rise to the vortical structures over the aftbody region. Kumar et al. [35] recently examined slender cones at high incidence. They showed that the onset of vortex asymmetry with nose-blunting correlates with geometrical parameters and is practically independent of Reynolds number.

Fidler [36] used active control of asymmetric vortices by rotating the nose, nose tip, and a band of the surface just aft of the nose on a pointed slender body at high angle of attack. Malcom et al. [37] manipulated forebody vortices to produce controlled yawing moments at high incidence on a generic fighter model. They used individually controlled forebody tip strakes with controlled blowing ports on the forebody to generate controlled yawing moments. Ng [38] and Stahl [39] used a single strake to suppress the vortex asymmetry on bodies of revolution, but Ng [38] showed that the small region close to the apex of the nose was the region of importance for control of vortex asymmetries. Ng and Malcom [40,41] used a rotatable miniature nose-tip strake and blowing and suction to produce controlled yawing moments on an F/A-18 model. Modi et al. [42] showed that delta strakes used as add-on tip devices could reduce side forces by over 95% for high incidences on a conical pointed forebody. Chen et al. [43] used nose-boom strakes on an F-16 model as an effective way of controlling forebody vortices at high angles of attack. Viswanath [44] studied different elliptic cones and showed that higher maximum side forces were obtained for a horizontal ellipse than for a vertical ellipse. Hodgkin and Wood [45] used tangential blowing on a generic fighter model to show increased yaw control above $\alpha = 60$ deg. A recent study by Patel et al. [46] developed a closed-loop flow control system for missile yaw stabilization and enhanced maneuverability. Dynamic experiments successfully demonstrated the ability of their closed-loop system to generate and maintain a range of desired yawing moments during high-alpha pitch sweeps. Leu et al. [47] incorporated flexible microballoon actuators in a slender cone cylinder and significantly reduced the side forces for some conditions.

III. Background: Source of Vortex Asymmetry at High Angles of Attack

In the aeronautical field, there have been several proposed source (s) of vortex asymmetry at high angles of attack. In 1971, Pick [48] speculated that large side forces and dynamic out-of-plane forces occurred at high angles of attack due to microasymmetries and geometrical imperfections near the nose. This premise would hint toward a boundary-layer-induced asymmetry in/near the location of flow separation, which would in turn cause an asymmetry in the vortex flowfield. This view can be supported by several experimental results. Investigations by Dexter and Hunt [49], Lamont [50], and Yanta and Wardlaw [51] presented detailed experiments showing the effect of roll angle on the flowfield and measured side forces. These studies showed that small changes in the roll angle of the nose/tip produced drastic changes in the asymmetric vortex pattern and measured side forces. Later, Zilliac et al. [29] assessed that the accumulation of dust on the tip region was enough to produce great changes in side-force variations.

In 1977, Keener and Chapman [52] suggested that the cause of vortex asymmetry is a hydrodynamic (inviscid) instability in the vortex flowfield that results from "the crowding together of the vortices as the apex angle is decreased." They indicated that "vortex crowding" occurs until the vortex pairs become unstable. At this moment, one of the vortices will slide up over the other vortex, hence inducing an asymmetric vortex flowfield. This hypothesis is supported to a certain degree by some experimental results, such as Keener and Chapman [53]. They found an estimation of the onset of vortex asymmetry on a pointed nose using the semi-apex angle and given by $\alpha_{\mathrm{AV}} = a\theta_A$. On the other hand, this postulated source of asymmetry (hydrodynamic instability) cannot be used to satisfactorily explain the large and dramatic changes in the side force and flowfield that occur with small changes in the tip/nose roll angle.

More recently, Degani and Schiff [27] and Degani [28] conducted Navier–Stokes simulations to successfully simulate the marked asymmetry that occurred experimentally on slender bodies of revolution at high angles of attack. They suggested that the source of asymmetry was a convective instability of the symmetric vortices. This conjecture could help explain the effect of different tip/nose roll angles on the measured side forces and flowfield. It is possible that different asymmetric vortex patterns could be produced by microasymmetries and geometrical imperfections near the nose as it is rotated. However, the convective instability premise cannot explain why the onset angle of attack varies with the nose-tip semi-apex angle or the reason for the existence of symmetric vortex pairs when the angle of attack is lower than the onset angle. Ng [38] showed that the small region close to the apex of the nose was the region of importance for control of vortex asymmetries. Ng also proposed that nose-blunting has the same effect of reducing the asymmetry as a strake, but with a different operating principle. The author indicated that blunting increased the distance between the two vortices.

IV. Characteristics of DEX

The basic premise of the DEX concept is that a small rocket-powered projectile is dispensed from an onboard flare dispenser upon detection of an incoming missile by the aircraft's warning system. The DEX is then maneuvered to engage and destroy the incoming enemy threat. Because of the high launch angles, the DEX can be subjected to large side forces as a result of forebody flow asymmetries, which can cause the projectile to spin out of control. Patel et al. [9] conducted a series of experimental and numerical investigations on optimizing the DEX design. They discussed two nose shapes: a hemispherical nose (hereafter, hemi-DEX) and an elliptical nose with an ellipticity of 0.33 (hereafter, e0.33-DEX). Results show that the forebody shape has a strong influence on the projectile's stability, and the effect of a forebody control device (strake) is dependent on the shape of the forebody.

One of the key characteristics of the DEX models is that both have a blunted nose that is not expected to produce a significant streamwise vortex pair, regardless of the angle of attack. The cylindrical aftbody is therefore the sole source of streamwise vortices. In the present case, the aftbody length is relatively short and therefore not likely to produce the multiple vortex pairs commonly observed on long slender bodies. As such, only a single pair of streamwise vortices is expected to occur on the cylindrical aftbody.

Because the noses on both models are rather blunt, significant asymmetric natural side forces may not be expected until fairly high angles of attack. Furthermore, the tail fins are large compared with the body length. Thus, in addition to the asymmetric pressure on the cylindrical body, vortex–fin interactions can be a source of side force and yawing moment.

V. Experimental Setup

A. Test Facility

Wind-tunnel experiments were performed at the University of Toledo's closed-loop circuit, single-return subsonic wind tunnel with a test section of 0.9×0.9 m (3×3 ft). The flow is driven by a 5-ft-diam, 14-blade, variable-pitch fan coupled to a 150-hp electric motor that allowed for speeds over 200 mph (89 m/s) in the test section. The tunnel is equipped with a C-strut model support and an automated turntable driven by an electric motor that allows for remote model positioning. By rotating the turntable, the angle of attack of the model can be varied up to 72 deg, and by sliding the model along the C-strut, the sideslip angle can be varied up to 56 deg without considerable interference of the C-strut or side walls on the upstream flowfield due to proximity effects.

Two-tempered glass sidewalls and a large Plexiglas window on the ceiling provided convenient access for flow visualization from different angles. The flow in the test section was uniform, with a turbulence level of 0.2% outside of the wall boundary layers. The tunnel is equipped with a five-component internal sting mount (balance) that allows for measurements of rolling, pitching, and yawing moments and normal and side forces. The sting was integrated with a custom-developed LabVIEW program that monitors test section conditions and measurements from the sting balance. Moment and force measurements were taken using a National Instruments SCXI unit integrated with a 4-Hz low-pass filter.

The facility is equipped with a 30-mW portable laser that is mounted on a Rhino three-degree-of-freedom traversing mechanism that allows the accurate positioning of the laser for laser-sheet visualizations. The smoke supplied to the test section is produced by a Rosco Delta 3000 remote-controlled fog machine. A reservoir-rake delivery system has been designed and fabricated, and smoke can be delivered in single or multiple jets through the use of a custom-made smoke rake. The smoke rake is mounted on a two-degree-of-freedom traversing mechanism that allows delivery of smoke to desired locations in the test section. The tunnel is equipped with an industrial blower that extracts smoke from the tunnel circuit.

B. Projectile Models

Figure 3 shows illustrations of the two projectiles examined: hemi-DEX (Fig. 3a, top) and e0.33-DEX (Fig. 3a, bottom) using a large fin-planform configuration, fin A. The only difference between the two designs is the forebody shape. In addition, experiments were conducted to examine the baseline (no control) flows and effects of an aftbody control device (strake) on the side force and yawing moments. A strake configuration optimization study was conducted in a separate effort, and results are reported by Lopera et al. [15]. The azimuthal and axial location of the strake for each configuration is shown in Fig. 3b.

Photos of the models with the sting are shown in Fig. 4. The models tested were 150% scale versions of the original 2-in.-diam, 8-in.-long DEX investigated by the U.S. Air Force [10–13], which results in a 3-in. model diameter and 12-in. model length. Each model consists of four fins, and all tests were conducted with fins in a cruciform (+) configuration. Additional wind-tunnel experiments were conducted on both projectile (hemi and e0.33) models using a smaller fin-planform configuration, hereafter termed fin B, to assess the effect of smaller fins on the side forces produced by baseline (clean body and no strakes) configurations. Figure 5 shows an illustration for the e0.33-DEX with the fin-B configuration. Furthermore, a configuration in which the four fins were removed from the hemi-DEX model, a "finless" configuration, was also examined.

C. Wind-Tunnel Experiments

The main objectives of the wind-tunnel experiments were to

1) Compare the aerodynamic forces and moments generated on the two baseline models (acquire C_M, C_y, and C_n).

2) Conduct detailed flow visualizations for the two DEX models at angles of attack of interest.

3) Compare and quantify the effects of an aftbody strake on both models.

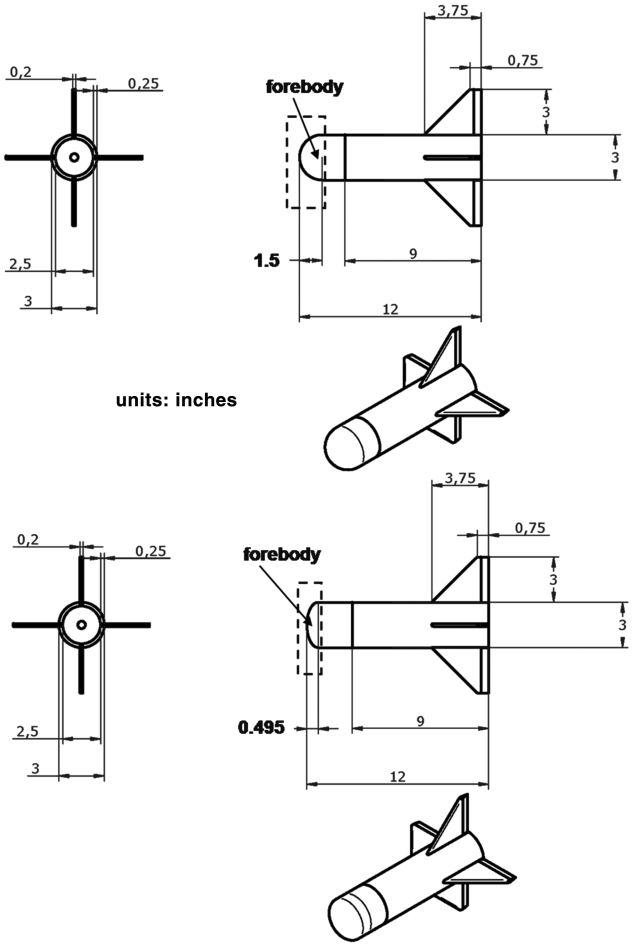

a)

strake configuration
- length = 1", (L_{strake}/L) = 0.083
- height = 0.5", (h_{strake}/D) = 0.167
- located at θ= 90 or 270°,
- 1.4" from the nose tip, (x/L) =1.2

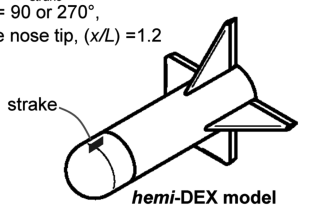

strake configuration
- length = 1", (L_{strake}/L) = 0.083
- height = 0.5", (h_{strake}/D) = 0.167
- located at θ= 90 or 270°,
- 1" from the nose tip, (x/L) = 0.083

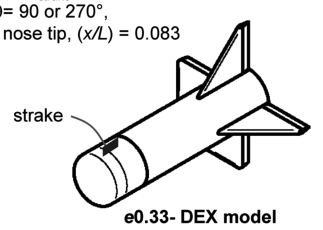

b)

Fig. 3 Shown are a) illustrations of the hemi-DEX (top) and e0.33-DEX (bottom) models with the fin-A configuration and b) details of the passive forebody strake (control device) used for yaw control experiments; the fin-A configuration was used on both DEX models.

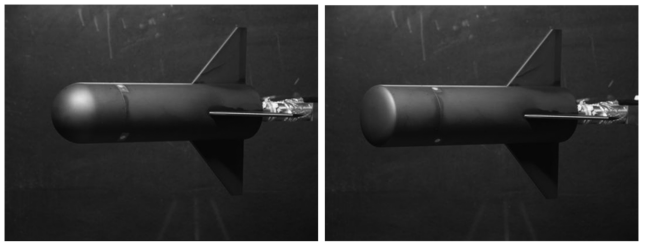

Fig. 4 Wind-tunnel picture of the hemi-DEX (left) and *e*0.33-DEX (right) models with the fin-A configuration.

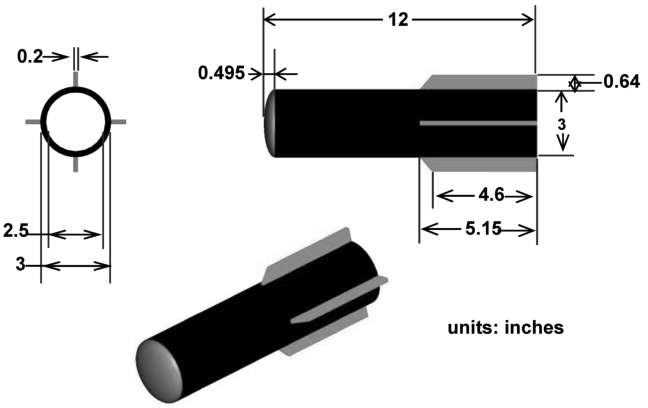

Fig. 5 Illustrations of the *e*0.33 DEX model with the fin-B configuration.

4) Correlate the flow interactions observed from flow visualization experiments with the force and moment data measured using the force balance.

Experiments were conducted at $U = 34$ m/s, $M = 0.1$, and the corresponding Reynolds number R_e of 0.19×10^6, based on the model diameter of 7.62 cm (3 in.). Static tests were conducted for $\alpha = 0$ to 64 deg at 2-deg increments with $\beta = 0$ deg. For all tests, 4000 samples were acquired at a sampling rate of 200 samples per second. Accuracy of force and moment data was verified by repeated measurements.

Two angles of attack, $\alpha = 42$ and 48 deg, were selected for both off-and-on- surface visualizations. These cases were selected based on force and moment measurements that show contrasting flow behaviors at the conditions. Off-surface flow visualization experiments were carried out using a smoke-and-laser-sheet method at $U = 8.8$ m/s. These experiments were conducted at a lower Reynolds number than the force measurement experiments so that there was sufficient smoke density in the test section to conduct detailed off-surface flow visualizations. On-surface flow visualizations were carried out using fluorescent oil, composed of a mixture of ZL-37 (Zyglo) and paint thinner, in conjunction with an industrial black-light lamp. These experiments were conducted at $M = 0.1$, with a corresponding $U = 34$ m/s.

VI. Force and Moment Results

Results are presented in the form of side-force coefficients and yawing- and pitching-moment coefficients. Azimuthal location for the flow effector (aftbody strake) tested is measured using a pilot's point of view, with $\theta = 0$ deg being the windward meridian (stagnation point) and increasing in a counterclockwise direction. Force and moment measurements were calculated with a reference point 14.3 cm (5.63 in.), or 47% model length, aft of the nose apex. Positive values for side-force and yawing-moment coefficients indicate a rightward side force and yawing moment, whereas negative values of side force and yawing moments indicate a leftward side force and yawing moment. For each baseline (no control) case, two tests were conducted and results are presented

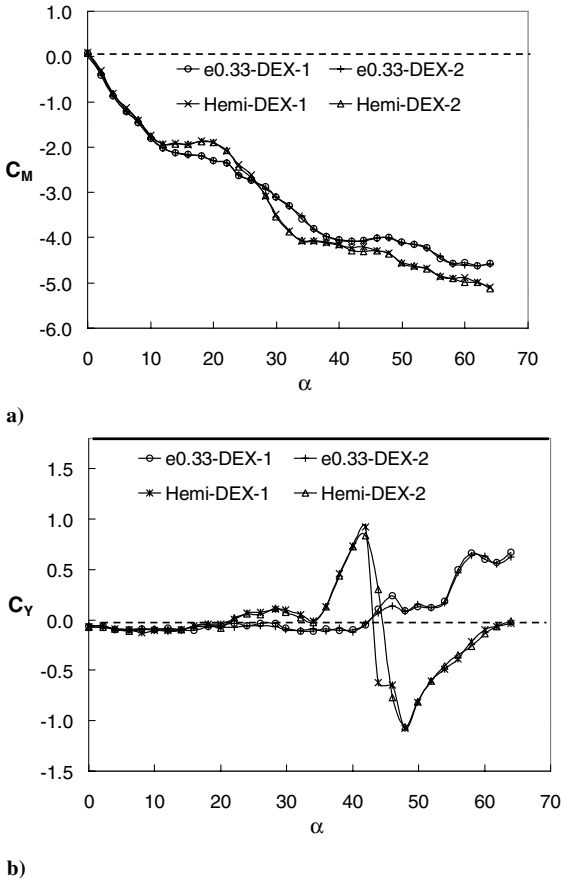

Fig. 6 Baseline DEX models at $M = 0.1$ and with the fin-A configuration: a) coefficient of pitching moment vs angle of attack and b) side-force coefficient vs angle of attack; + values indicate a rightward side force and − values indicate a leftward side force.

showing the two test cases (1 and 2) for each configuration, to show the repeatability obtained for the forces and moments measured. The average 95% confidence level was ± 0.0118 for the pitching-moment coefficient and ± 0.012 for the yawing-moment coefficient.

A. Baseline Results

Figure 6a shows results of pitching-moment coefficients for the baseline (no strake) cases for the hemi-DEX and *e*0.33-DEX models. The pitching-moment characteristics for both projectile configurations indicate a nose-down pitch control over the entire α range tested. The difference in the pitching-moment curves is a result of the different forebody geometries. Because the *e*0.33-DEX has a larger projected area forward of the moment reference, all else being equal, one may expect the geometry to favor a lower overall nose-down pitching moment compared with the hemi-DEX. This is borne out by the pitching moment for *e*0.33-DEX showing a more gradual increase in nose-down pitching moment with increasing incidence in comparison with the hemi-DEX and by the hemi-DEX having a larger nose-down pitch than the *e*0.33-DEX for α greater than 25 deg. The exception is between $\alpha = 12$ and 24 deg, for which the *e*0.33-DEX shows a lower nose-down moment than the hemi-DEX, which suggests that the flow around the hemispherical nose produces a higher local lift.

Results for side-force coefficients are shown in Fig. 6b. The hemi-DEX model shows significant asymmetric side forces from $\alpha = 34$ to 60 deg. The side force switches from a rightward (positive) force at 42 deg to a leftward (negative) force at 48 deg. The *e*0.33-DEX shows a small side force to the left for $\alpha = 0$ to 42 deg. For $\alpha = 44$ to 54 deg, the *e*0.33-DEX showed a small rightward force with small oscillations. The side force increases rapidly in magnitude from $\alpha = 54$ to 64 deg. The maximum side force measured for the *e*0.33-DEX was, however, 45 to 65% lower than the maximum side forces for the hemi-DEX.

An estimation on the onset of aftbody vortex asymmetry can be made using the correlation $\alpha_{AV} \sim 4.2(D/L)$ [54], which gives a value of approximately 60 deg for the two projectile models. The observed side-force behavior for the *e*0.33-DEX agrees well with this estimation. On the other hand, with the onset of asymmetry at $\alpha = 34$ deg, the hemi-DEX exhibits a behavior that is more akin to a pointed-nose body. An estimation of the onset of vortex asymmetry on a pointed nose is given by $\alpha_{AV} = 2\theta_A$ [53,55]. The measured α_{AV} for the hemi-DEX is 34 deg, which gives an effective θ_A of 17 deg. Also of interest is the diminishing of the asymmetric side force for the hemi-DEX at around $\alpha = 60$ deg, which is exactly opposite from the expectation for a blunt-nose body. The disappearance of an asymmetric side force at high angles of attack on a pointed body is most often a result of the advancement of vortex breakdown. In summary, the hemi-DEX behaves more like a pointed-nose body than a blunt-nose body.

B. Effect of Fins on Side Force

Results for side-force coefficients for baseline cases showed that the hemi-DEX model generated large side forces that switched direction (rightward side force to leftward side force) at $\alpha = 42$ and 48 deg. In contrast, the *e*0.33-DEX model did not show this trend in side-force direction reversal. To assess the effect of fins on the side forces produced by the projectile models, experiments were conducted using a smaller fin planform, fin B. Figure 7 shows side-force coefficients for both projectile models using a smaller fin planform, fin B. Results show that a large rightward side force is produced by the hemi-DEX model at $\alpha = 40$ deg, and it switches direction to a leftward side force at $\alpha = 46$ deg. The magnitude of the side forces produced at these two angles of attack is almost identical, but opposite in direction. The *e*0.33-DEX model shows nearly negligible side forces up to $\alpha = 56$ deg. These results shows that the large side forces produced on the hemi-DEX model persist even with a significantly smaller fin-planform configuration, and the smaller fin size has the effect of precipitating the onset of large out-of-plane forces by a 2-deg angle of attack. Results for the *e*0.33-DEX model follow a similar trend for both fin configurations, with the appearance of a large side force at $\alpha = 56$ deg.

After reviewing results for both DEX models and fin configurations, a further investigation of a hemi-DEX model with a finless configuration (all four fins were removed) was conducted and results are shown in Fig. 8. Results show the persistence of a large rightward side force that reverses direction to a leftward side force at $\alpha = 42$ and 50 deg. The rightward side force measured at $\alpha = 42$ deg is approximately 50% higher than the leftward side force measured at $\alpha = 50$ deg, but both side forces are large in magnitude ($C_Y > \sim|1|$). This result would indicate that the large side forces previously measured on the hemi-DEX model are produced mainly by the hemispherical forebody, and there is little fin interaction with the leeward vortices affecting the produced side forces. For the three hemi-DEX configurations examined (fin *A*, fin *B*, and finless), the α and direction of the maximum measured side forces are similar, with their onset angles being within a ± 2-deg angle of attack and with the same force direction reversal (rightward to leftward). The side-force magnitude is almost identical for the hemi-DEX with fin-A and fin-B configurations and has a bias to a larger rightward side force for the finless configuration.

C. Yaw Control Results

Effects of an aftbody strake on the side force and yawing moment was examined for both designs. A parametric study to optimize the strake parameters for yaw control at high angles of attack was performed by Lopera et al. [15]. The study revealed that the most effective aftbody strake configuration, designated as strake B, was a "rectangular" strength with a length of 1–in. ($L_{strake}/L = 0.083$) and a height of 0.5 in. ($h_{strake}/D = 0.167$). The optimum azimuthal and axial strake locations for the *e*0.33-DEX was found to be 1 in. ($x/L = 0.083$) aft of the nose apex and at 90 or 270 deg (i.e., right and left meridians). For the hemi-DEX, experiments herein revealed that the optimum strake location for the hemi-DEX was 1.4 in. ($x/L = 0.12$) aft of the nose apex at the same azimuthal locations ($\theta = 90$ or 270 deg).

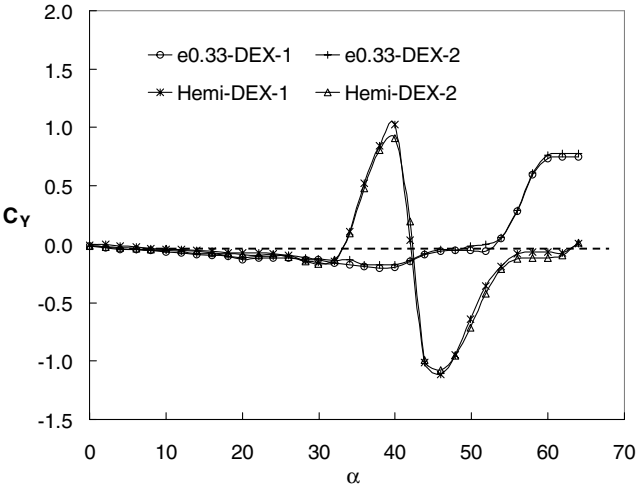

Fig. 7 Side-force coefficient vs angle of attack for the baseline DEX models at $M = 0.1$ and with the fin-B configuration; + values indicate a rightward side force and − values indicate a leftward side force.

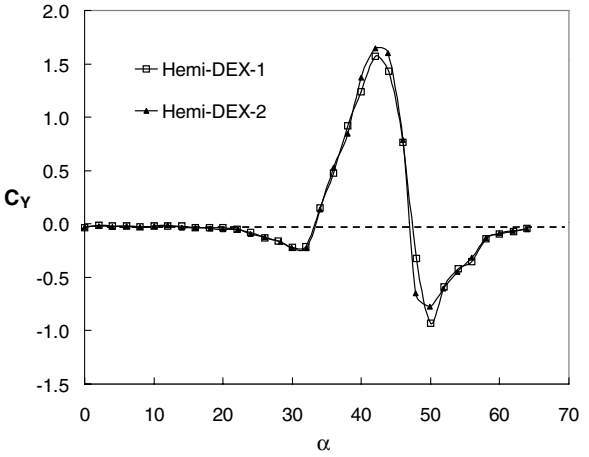

Fig. 8 Side-force coefficient vs angle of attack for the baseline finless hemi-DEX model at $M = 0.1$; + values indicate a rightward side force and − values indicate a leftward side force.

Results for side-force and yawing-moment coefficients are shown in Fig. 9. Figure 9a shows that for α greater than 42 deg, the controlled side force achieved by a single strake on the aftbody of the hemi-DEX is larger than for the *e*0.33-DEX. The maximum side force attainable with a single strake at $\theta = 90$ or 270 deg on the hemi-DEX was almost 50% larger than that on the *e*0.33-DEX under similar conditions. For both models, the side forces obtained by a single aftbody strake on the right meridian ($\theta = 90$ deg) were similar in magnitude but opposite in direction to that achieved using a single aftbody strake on the left meridian ($\theta = 270$ deg). Figure 9b shows the yawing-moment coefficients for baseline and control cases for $\alpha = 30$ to 64 deg. Results show that above $\alpha = 50$ deg, the effects of a single aftbody strake on the hemi-DEX produced yawing moments 20–50% larger than with the *e*0.33-DEX model. It can be seen that the yawing moment follows the same trend as the side force. This indicates that the center of force stays ahead of the moment reference point through the range of angle of attack tested. In all cases, the yawing moment maintains a proportionally high value compared with the dropoff in the side force with increasing angles of attack, thereby indicating a forward shift in the center of force.

VII. Flow Visualization Results

Force and moment results show significant differences between behaviors of the hemi-DEX and *e*0.33-DEX projectiles at high

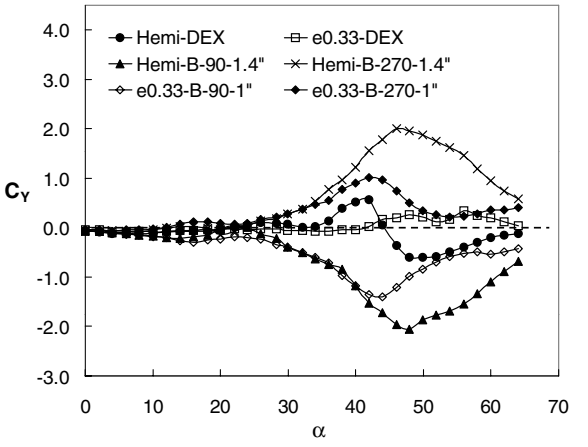

a)

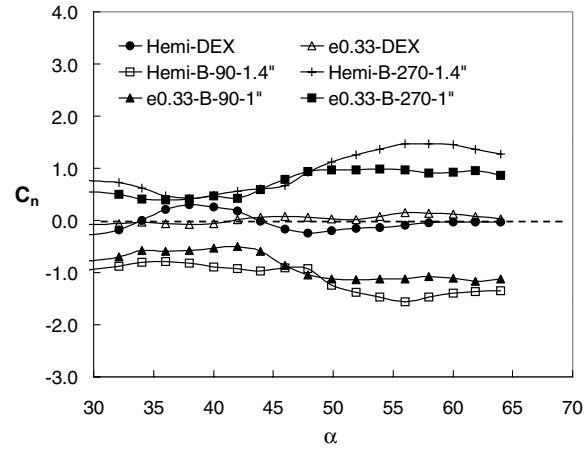

b)

Fig. 9 Effect of different aftbody strake patterns on the DEX models at $M = 0.1$ and with the fin-A configuration: a) side-force coefficient vs angle of attack and b) yawing-moment coefficient vs angle of attack.

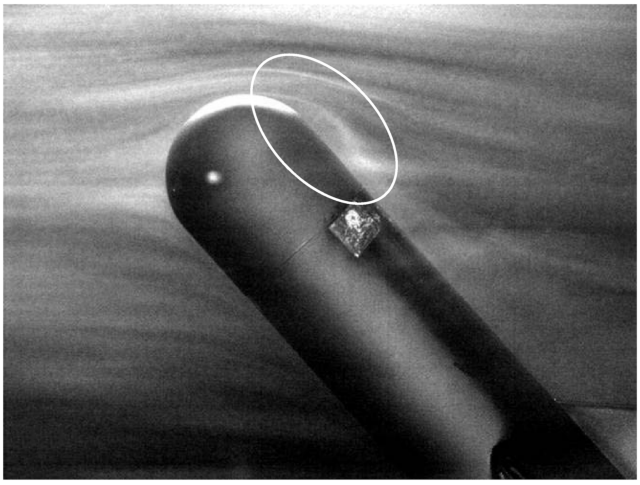

a)

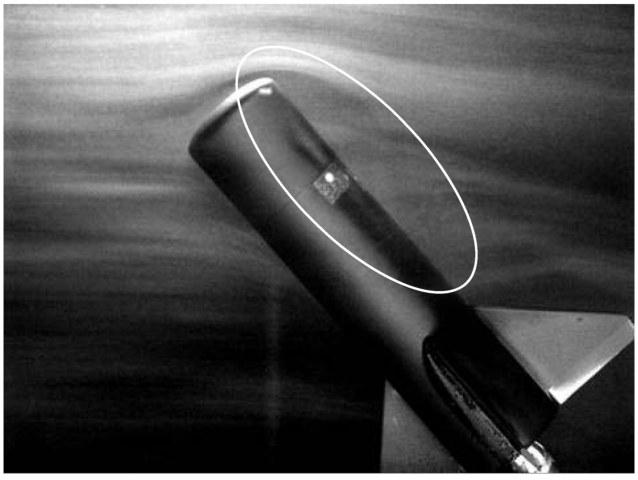

b)

Fig. 10 Smoke-stream visualizations at $\alpha = 48$ deg, $\beta = 0$ deg, $U = 8.8$ m/s, and with the fin-A configuration: a) hemi-DEX and b) *e*0.33-DEX.

incidence. The baseline flows and strake-induced behaviors are examined herein through visualizations of the flowfield using the fin-A configuration on both projectile models. The discussions will focus on the roles of forebody geometry and streamwise vortices.

A. Off-Surface Visualizations

1. Baseline Cases

To study the flowfield around the two projectile models, off-surface flow visualizations were performed at $\alpha = 42$ and 48 deg. These conditions were selected based on the side-force results that showed rather different behaviors for the two models at these angles of attack.

Smoke-stream visualizations of the flowfield obtained at $\alpha = 48$ deg are shown in Figs. 10a and 10b for the hemi-DEX and *e*0.33-DEX models, respectively. Figure 10a shows that on the hemi-DEX, the smoke stream separates in the leeward region from the hemispherical nose around 70 to 80 deg (0 deg being the center axis of the projectile and in the same plane as the horizontal fins), and the flow reattaches downstream to create a recirculation bubble that is between 2 ($L_{rb}/L = 0.167$) and 2.5 in. long ($L_{rb}/L = 0.208$). In contrast, Fig. 10b shows that on the *e*0.33-DEX, the smoke stream separates from the surface in front of the elliptical nose and the flow does not reattach to create a recirculation bubble. Also seen are a steady vortex pair shedding off the cylindrical aftbody, and at $\alpha = 48$ deg, the core of the vortices appears to have just cleared the top of the vertical tail fin.

Laser-sheet visualizations were conducted for the hemi-DEX and *e*0.33-DEX projectiles at five different cross-sectional stations along the length of the model. Figure 11 shows the locations of the laser-sheet cross-sectional stations. Location 1 was a cross-sectional plane located at 0.5 in. ($x/L = 0.042$) aft of the nose apex, location 2 was at 1.5 in. ($x/L = 0.13$), location 3 was at 2.5 in. ($x/L = 0.21$), location 4 was at 4 in. ($x/L = 0.33$), and location 5 was at 5 in. ($x/L = 0.42$). Representative results of the flowfield for both projectile models are discussed.

Figure 12 shows visualizations at different laser-sheet cross sections for the hemi-DEX model at $\alpha = 42$ deg. Side-force measurements acquired at 42 deg indicate the presence of a large rightward (positive) side force of the model. Figure 12a shows a distinct separated flow region at station 2 ($x/L = 0.13$). Furthermore, below the separated flow region, the outline of two vortices (sketched in Fig. 12a) can be observed on the leeward surface. At station 5 ($x/L = 0.42$), Fig. 12b shows two well-defined counter-rotating vortices rolling off the leeward surface of the hemi-DEX. This image shows that the vortices are fairly symmetric. One would expect, based on the side-force results at $\alpha = 42$ deg, that the right vortex would be closer to the body and the left vortex would be either weaker than the right vortex or that it would be positioned farther away from the leeward surface than the right vortex. These expected vortex patterns are not clearly visible in Fig. 12b.

At $\alpha = 48$ deg, side-force measurements showed a large leftward (negative) side force for the hemi-DEX. Figure 13 shows laser-sheet visualization for the hemi-DEX at $\alpha = 48$ deg. At station 2, Fig. 13a shows that there is still a distinct separated region in the front portion of the hemi-DEX. Concurrently, a pair of vortices is observed over the leeward surface below the separated region. The outline of the vortices is sketched in the figure. The vortices are well-separated from each other and are lifted off the leeward surface a significant

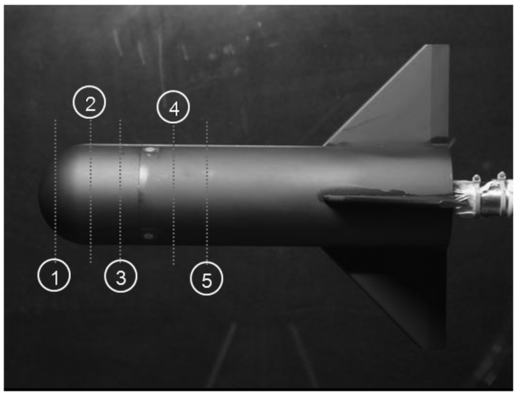

Fig. 11 Cross-sectional stations used for laser-sheet visualizations of the fin-A configuration.

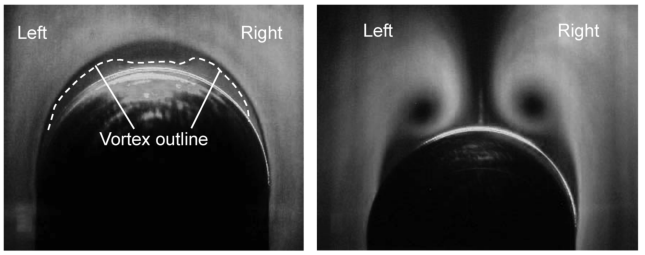

a) b)

Fig. 12 Laser-sheet visualizations for the hemi-DEX model at $\alpha = 42$ deg, $\beta = 0$ deg, $U = 8.8$ m/s, and with the fin-A configuration: a) station 2 ($x/L = 0.13$) and b) station 5 ($x/L = 0.42$); pilot's point of view.

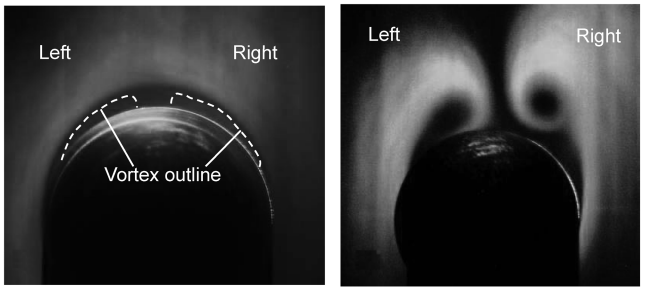

a) b)

Fig. 13 Laser-sheet visualizations for the hemi-DEX model at $\alpha = 48$ deg, $\beta = 0$ deg, $U = 8.8$ m/s, and with the fin-A configuration: a) station 2 ($x/L = 0.13$) and b) station 5 ($x/L = 0.42$); pilot's point of view.

distance. On the hemi-DEX aftbody, Fig. 13b shows that at station 5 ($x/L = 0.42$), the left vortex stays close to the leeward surface, whereas the right vortex can be seen to lift above the left vortex and away from the leeward surface. The vortex pattern correlates well with the large leftward (negative) side force measured (see Fig. 6b).

Laser-sheet visualizations of the $e0.33$-DEX model are presented in Figs. 14 and 15. At $\alpha = 42$ deg, side-force measurements showed negligible effects, which would indicate that the flowfield, including the vortex pair, of the leeward region of the $e0.33$-DEX is mostly symmetric. Figure 14 shows a laser-sheet cross section of the $e0.33$-DEX model at $\alpha = 42$ deg. These images show a pair of counter-rotating vortices over the leeward region of the model. The two counter-rotating vortices are significantly closer to the leeward surface than those observed on the hemi-DEX. The vortices over the $e0.33$-DEX are also more closely spaced compared with the hemi-DEX vortices, and the vortex core is not as well-defined and the circulation is not as strong as that observed on the hemi-DEX. Another noticeable trend is that the vortex pair is symmetric,

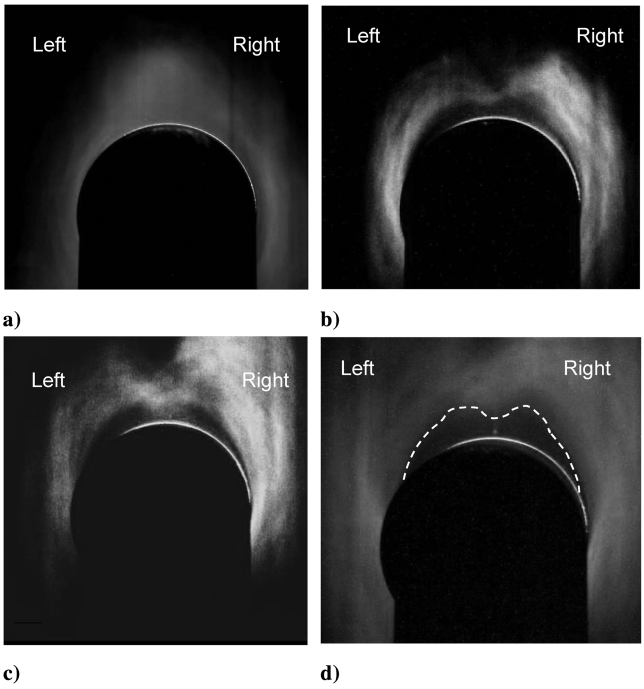

a) b) c) d)

Fig. 14 Laser-sheet visualizations for the $e0.33$-DEX model at $\alpha = 42$ deg, $\beta = 0$ deg, $U = 8.8$ m/s, and with the fin-A configuration: a) station 2 ($x/L = 0.13$), b) station 3 ($x/L = 0.21$), c) station 4 ($x/L = 0.33$), and d) station 5 ($x/L = 0.42$); pilot's point of view.

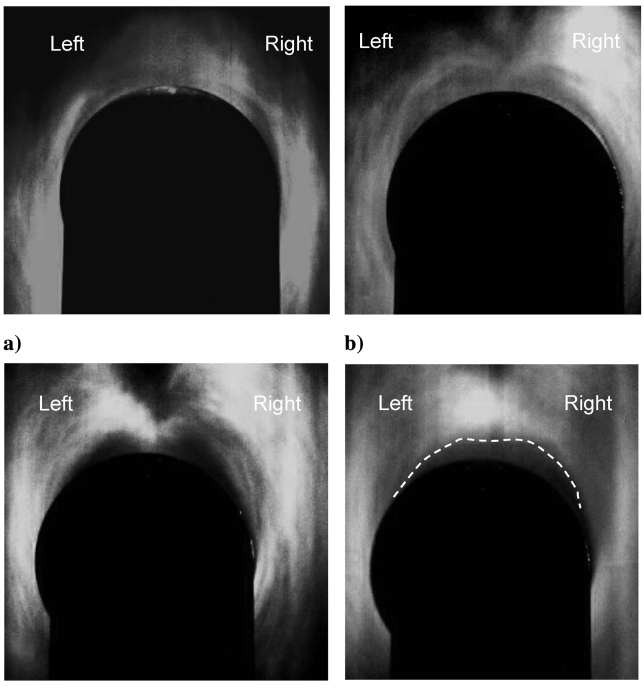

a) b) c) d)

Fig. 15 Laser-sheet visualizations for the $e0.33$-DEX model at $\alpha = 48$ deg, $\beta = 0$ deg, $U = 8.8$ m/s, and with the fin-A configuration: a) station 2 ($x/L = 0.13$), b) station 3 ($x/L = 0.21$), c) station 4 ($x/L = 0.33$), and d) station 5 ($x/L = 0.42$); pilot's point of view.

indicating that the left- and right-side vortices do not produce a significant net side force, which correlates well with acquired static side-force measurements. Furthermore, a comparison of the cross sections at station 2 ($x/L = 0.13$) for both models at $\alpha = 42$ deg, shown in Figs. 12a and 14a, illustrate some important physical differences. Figure 12a shows a separated region that is very defined, which is consistent with the recirculation bubble observed for the

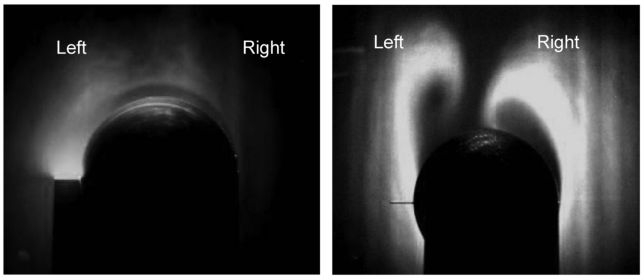

a) b)

Fig. 16 Laser-sheet visualizations of an aftbody strake on the hemi-DEX model at $\alpha = 48$ deg, $\beta = 0$ deg, $U = 8.8$ m/s, and with the fin-A configuration: a) station 2 ($x/L = 0.13$) and b) station 5 ($x/L = 0.42$); pilot's point of view.

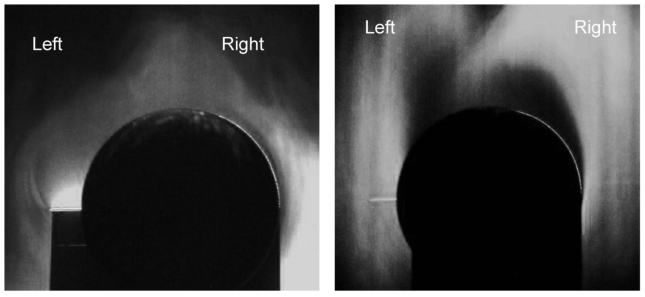

a) b)

Fig. 17 Laser-sheet visualizations of an aftbody strake on the *e*0.33-DEX model at $\alpha = 48$ deg, $\beta = 0$ deg, $U = 8.8$ m/s, and with the fin-A configuration: a) station 2 ($x/L = 0.13$) and b) station 5 ($x/L = 0.42$); pilot's point of view.

hemi-DEX model in Fig. 10a. In contrast, a cross section of the *e*0.33-DEX, shown in Fig. 14a, depicts a large blurred region in which no clear recirculation pattern can be identified, and traces of a pair of counter-rotating vortices are faintly distinguishable over the leeward surface. The result shown in Fig. 14a is consistent with the separated flow (mostly dead air) region behind the elliptical forebody shown in Fig. 10b.

Side-force measurements for the *e*0.33-DEX model at $\alpha = 48$ deg show a very small rightward (positive) side force. Laser-sheet cross sections of the elliptical DEX model at $\alpha = 48$ are presented in Fig. 15. Visualizations obtained at $\alpha = 48$ deg show trends similar to those observed for the *e*0.33-DEX at $\alpha = 42$ deg. Figures 15b and 15c show a pair of counter-rotating vortices over the leeward surface of the model that are fairly close to the leeward surface, and the spacing distance between the two vortices is substantially smaller than that of the vortices on the hemi-DEX model. This vortex pair seems to be symmetric, with the left- and right-side vortices being the same distance away from the leeward surface. The vortex cores are not easily distinguishable, as was the case on the hemi-DEX model. By comparing the cross-sectional views from station 2, one can distinguish the large difference in separation patterns behind the two different forebodies examined. Figure 13a shows a well-defined separated region, which is consistent with the smoke-stream visualization shown in Fig. 10a that shows a recirculation bubble behind the hemispherical forebody. In contrast, Fig. 15a shows a separated region for the *e*0.33-DEX that is not as clear and well-defined as for the hemi-DEX, and the outline of two leeward vortices is very close to the surface. The outer region of *blurred and disorganized* flow is consistent with smoke-stream visualization presented in Fig. 10b at the same incidence.

2. *Yaw Control Cases*

The effect of an aftbody strake on the yaw control and the flowfield around the two projectile models is examined. The same five cross-sectional stations shown in Fig. 11 were used for flow visualization. Side-force and yawing-moment coefficients induced by a strake at $\alpha = 48$ deg on both DEX models were previously discussed. Figure 16 shows different laser-sheet visualizations for the hemi-DEX model, with a strake mounted at $\theta = 270$ deg for $\alpha = 48$ deg. Figure 16a shows the separated flow over the strake that distorts the recirculation bubble over the nose. The separated flow forms a vortex over the strake. The strake vortex serves as an initiation for the main left vortex and induces the left vortex to lift off and separate from the surface. Correspondingly, the right vortex moves from its natural (uncontrolled) position toward the leeward surface. At stations 5 ($x/L = 0.42$), Fig. 16b shows that the left vortex (strake side) is substantially farther from the surface than is the right vortex. Side-force measurements, for which a strake placed on the left meridian generated a large side force to the right side for the hemi-DEX model for $\alpha > 20$ deg, correlate well with these visualizations.

Laser-sheet visualizations of the *e*0.33-DEX model with a single strake placed in the left meridian, $\theta = 270$ deg, are shown in Fig. 17. Behaviors of the flow are similar to those of the hemi-DEX. Even though the hemi-DEX flow appears to have a somewhat better defined vortex core than the *e*0.33-DEX, the two controlled flows show a significantly lower level of difference between them compared with that between the baseline flows.

B. Surface Visualizations

Surface visualizations were conducted for both projectile baseline models at $\alpha = 42$ and 48 deg using the fin-A configuration. Surface visualizations were conducted from three views: 1) top view, 2) left-side view, and 3) right-side view.

1. *Hemi-DEX Model*

Figures 18 and 19 show surface visualization results of the hemi-DEX model. Side-force results in Fig. 6b indicate that at $\alpha = 42$ deg, the hemi-DEX produces a large rightward side force. Figures 18a and 18b show a top view of the hemi-DEX at $\alpha = 42$ deg. This picture clearly shows the three-dimensional primary separation that occurs on the hemi-nose. A second oil line, shortly downstream of the primary separation line but well upstream of the reattachment point identified in Fig. 10a, can also be seen clearly. This second oil line indicates the forebody secondary separation line. The forebody flow reattachment point is observed well aft of the forebody secondary separation line and is located close to the attachment point observed for the separation bubble in Fig. 10a. Furthermore, the left-side secondary separation line is observed to extend along the body in a fairly straight manner, whereas the right-side secondary separation line is closer to the leeward meridian and in the aftbody shows a wavy pattern. The influence of the tail fins is also evident.

From the surface visualizations for the left and right sides, shown in Figs. 18c and 18e, respectively, it can be determined that the flow in the right side remains attached to the body up to a larger azimuthal angle θ than does the left side. This correlates well with the rightward side force measured at $\alpha = 42$ deg, showing that the flow in the right side remains attached to a significantly larger azimuthal angle than on the left side, thereby generating a rightward side force on the model. Figures 18c and 18d also shows the 3D primary and secondary separations of the hemi-DEX forebody. The surface imprint of the tertiary vortex over the cylindrical aftbody is also clearly visible. From this imprint, it can be deduced that the primary vortex starts forming just downstream of the hemispherical nose, causing a distinct kink in the separations lines of the nose bubble. Of particular interest is the apparent merging of the secondary flow of the nose and the aftbody (tertiary) vortex. This suggests that the recirculation flow over the nose can potentially provide a communication link between the left and right aftbody vortices.

Surface visualizations for the hemi-DEX model at $\alpha = 48$ deg are shown in Fig. 19. Side-force results presented in Fig. 6b indicate that at $\alpha = 48$ deg, the hemispherical model produces a large leftward side force. Figures 19a and 19b show the 3D separation and reattachment over the hemi-DEX forebody. This phenomenon is also observed in Fig. 10a as a recirculation bubble. As observed at $\alpha = 42$ deg, there is a noticeable difference in the separation patterns on the aftbody for the left and right sides. Furthermore, there is a small local region of recirculation on the left side behind the

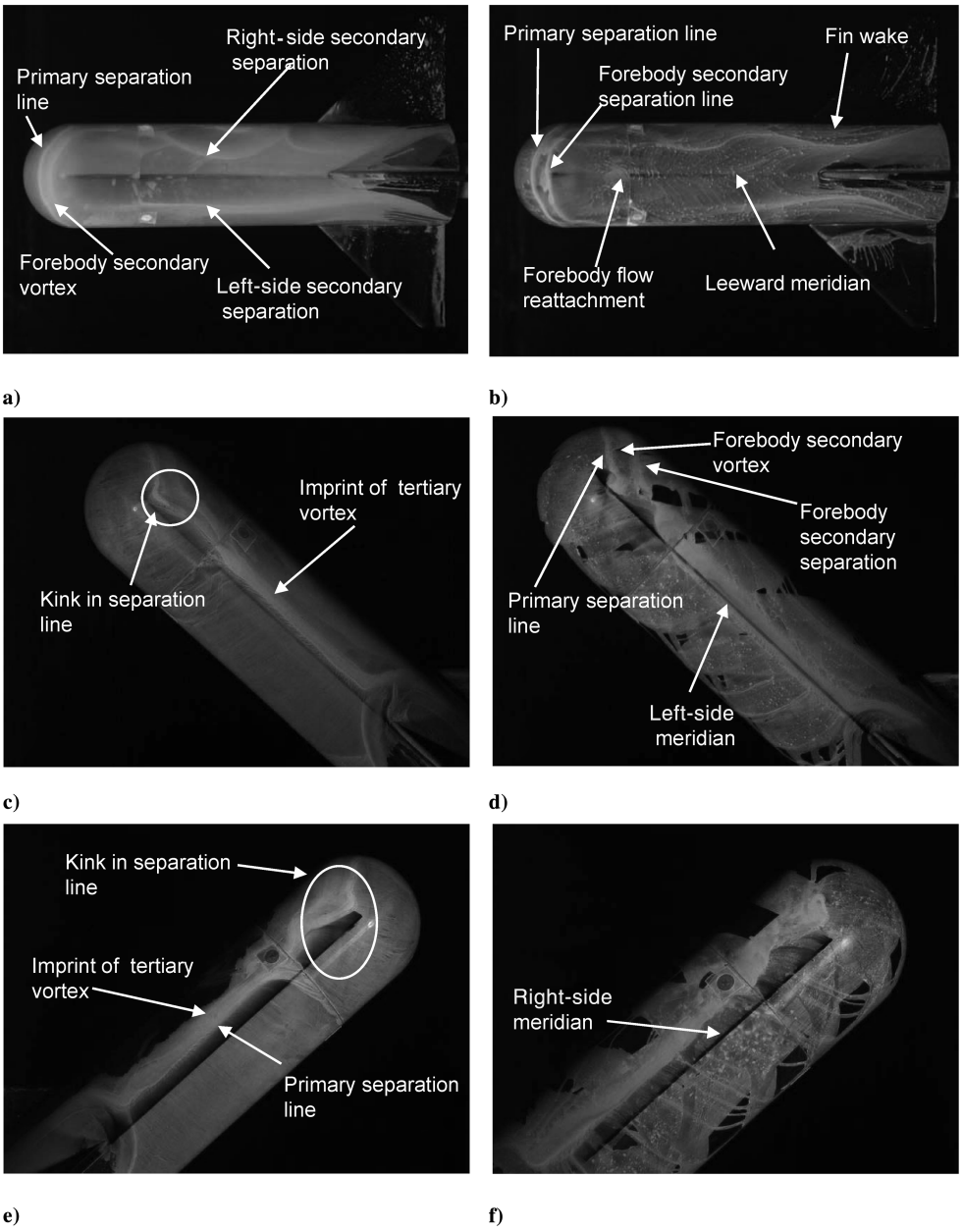

Fig. 18 Oil-surface visualizations for the hemi-DEX model at $\alpha = 42$ deg, $\beta = 0$ deg, $U = 34$ m/s, and with the fin-A configuration: a) top view, b) left-side view, and c) right-side view.

recirculation bubble (see Fig. 19a). There also appears to be less influence from the tail fins.

Figures 19c and 19d show that there is a local recirculation region on the left side behind the recirculation bubble over the hemi-DEX forebody, similar to that observed in Fig. 19a. This second region of recirculation shows strong activity and unsteadiness. In addition, the flow in the left side of the aftbody appears to separate near the left-side meridian. Surface visualization of the right side, shown in Figs. 19e and 19f, shows a 3D primary separation, and a kink is also clearly visible in the separation lines of the forebody and aftbody flows. Of particular interest is the apparent merging of the secondary flow of the nose and the aftbody (tertiary) vortex. As observed at $\alpha = 42$ deg, this suggests that the recirculation flow over the nose can potentially provide a communication link between the left and right aftbody vortices. A local recirculation region such as the one observed on the left was not observed on the right side. The flow on the right side of the aftbody separates some distance above the right-side meridian. These results are somewhat conflicting because the measured large leftward side force at $\alpha = 48$ deg would indicate that the flow would separate later on the left side than on the right side. An important consideration is that the side flow visualizations were obtained with the model at a different orientation in the wind tunnel from that for force measurements. For side-view surface visualizations, the model was positioned at $\alpha = 42$ and 48 by sliding it along the C-strut, and for force measurements, it was positioned by rotating the turntable and keeping it parallel to the flow with respect to the C-strut initial orientation.

2. *e*0.33-*DEX Model*

Surface visualizations for the *e*0.33-DEX model are shown in Figs. 20 and 21 for $\alpha = 42$ and 48 deg, respectively. At $\alpha = 42$ deg, side-force data indicate a negligible side force. Figures 20a and 20b show a distinct primary separation line and traces of oil accumulation behind it, which are interpreted as an imprint of the aftbody vortex. In addition, the oil streakline patterns in the leeward surface appear to be mostly symmetric, as expected for a case with negligible side force. The aftbody vortices appear to start forming just downstream of the nose. Strong regions of flow recirculation can be observed on the left and right sides upstream of the tail fins.

Side-force measurements for the *e*0.33-DEX model at $\alpha = 48$ deg showed a very small side force to the right side. Figure 21a

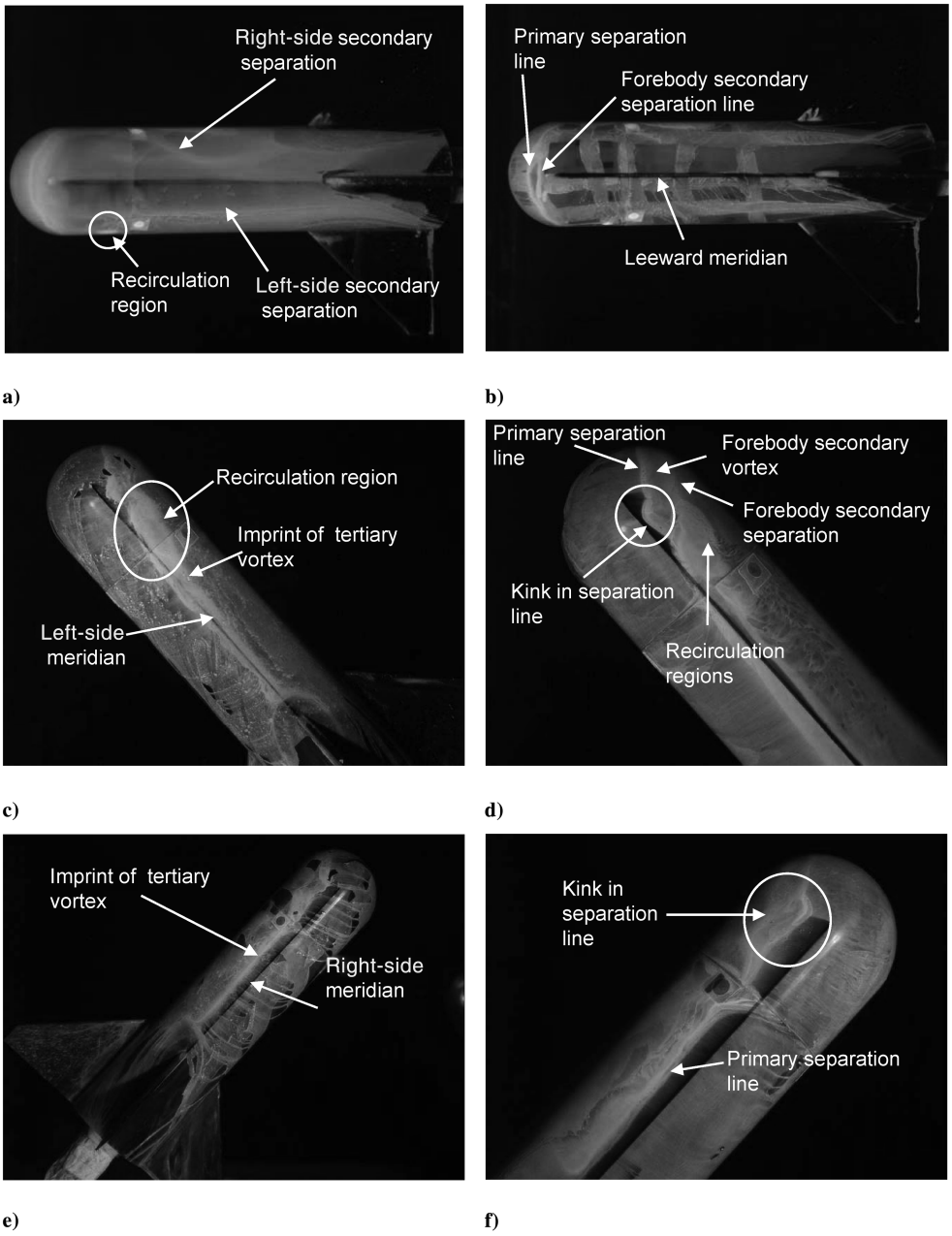

Fig. 19 Oil-surface visualizations for the hemi-DEX model at $\alpha = 48$ deg, $\beta = 0$ deg, $U = 34$ m/s, and with the fin-A configuration: a) top view, b) left-side view, and c) right-side view.

shows a distinct primary separation line and, behind it, a region of symmetric skin-friction lines. These results are consistent with smoke-stream visualizations at the same α, presented in Fig. 10b. Figure 21b shows the primary separation line in front of the $e0.33$-DEX nose. This separation appears to be strong and global. Figures 21b and 21c also show some large regions of recirculation on the left and right surfaces of the aftbody.

VIII. Vortex Breakdown Investigations

Vortex breakdown is an important practical phenomenon in aeronautics and can sometimes limit the operating attitude of slender-winged air vehicles. Laser-sheet flow visualizations were conducted on both projectile models using the fin-A configuration to assess the effect of the two blunt forebodies on vortex breakdown. Visualizations were conducted at $\alpha = 48$ deg, $\beta = 0$ deg, and $U = 8.8$ m/s. Figure 22 shows the locations of the laser-sheet cross-sectional stations examined. Location 5 was a cross-sectional plane located at 5 in. ($x/L = 0.42$) aft of the nose apex, location 6 was at 5.5 in. ($x/L = 0.46$), location 7 was at 6 in. ($x/L = 0.5$), location 8 was at 6.5 in. ($x/L = 0.54$), location 9 was at 7 in. ($x/L = 0.58$), and location 10 was at 7.5 in. from the nose apex ($x/L = 0.625$).

A. Hemi-DEX Model

Representative results from off-surface visualization records for the hemi-DEX model are shown in Fig. 23. At cross-sectional station 6 ($x/L = 0.46$), Fig. 23a shows that there are two distinct counter-rotating vortices over the leeward side of the hemi-DEX. The vortex cores for the left- and right-side vortices are well-defined. Results for visualizations at cross-sectional stations farther aft of the nose show a similar trend in the existence of a well-defined and strong counter-rotating vortex pair over the leeward surface of the hemi-DEX. At station 10 ($x/L = 0.625$), Fig. 23b shows that strong vortex cores are still evident on the aftbody region close to the fins. Furthermore, results from oil-surface visualizations conducted at similar conditions (see Fig. 19) did not show imprints of vortex breakdown, commonly distinguished in surface patterns as areas with a well-defined foci and strong recirculation regions, on aftbody

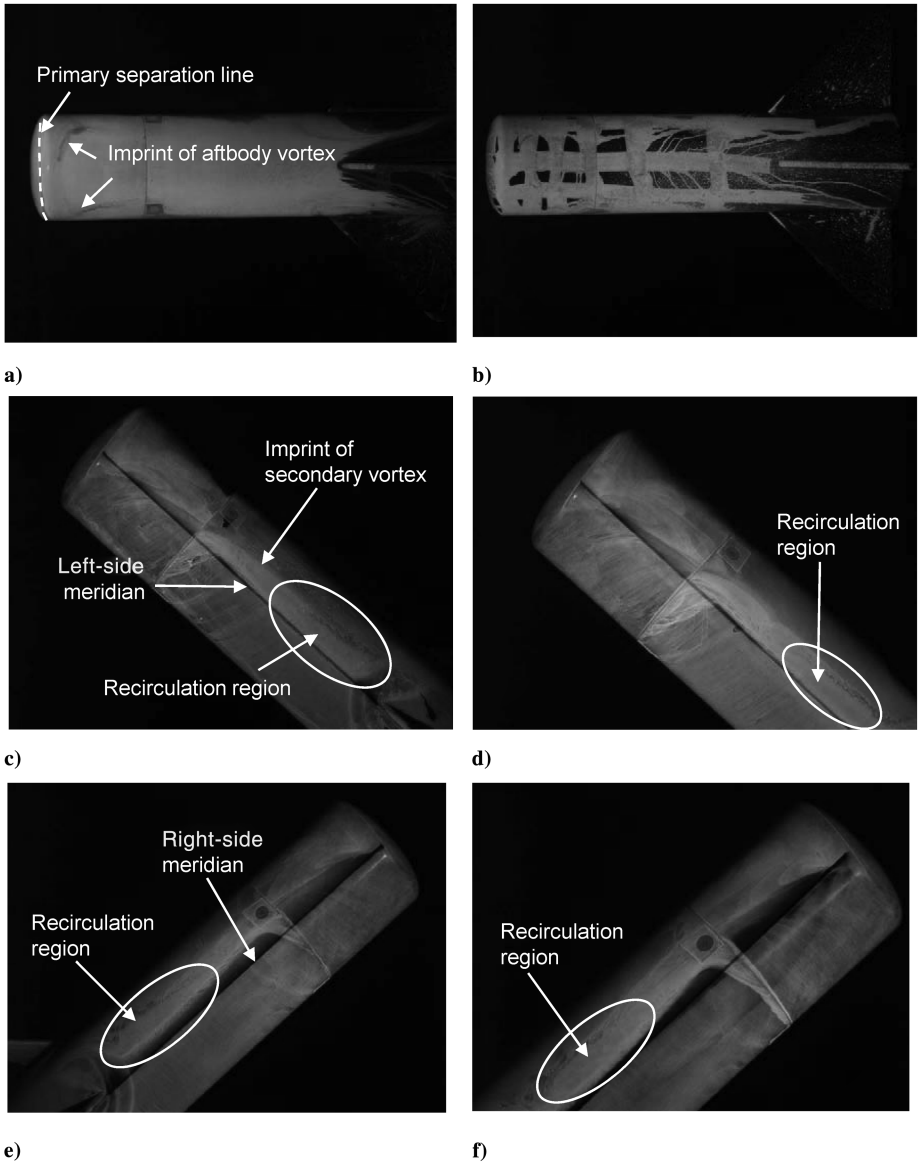

Fig. 20 Oil-surface visualizations for the e0.33-DEX model at $\alpha = 42$ deg, $\beta = 0$ deg, $U = 34$ m/s, and with the fin-A configuration: a) top view, b) left-side view, and c) right-side view.

surface patterns. These results indicate that vortex breakdown does not appear to occur for the hemi-DEX model at $\alpha = 48$ deg.

B. e0.33-DEX Model

Representative results from off-surface visualization records for the e0.33-DEX model are shown in Fig. 24. At cross-sectional station 5 ($x/L = 0.42$), Fig. 24a shows that the vortex cores of the pair of counter-rotating vortices over the leeward surface of the aftbody are substantially weaker than those observed for the hemi-DEX model and are difficult to observe. At similar conditions, the vortex cores on the hemi-DEX leeside were clearly distinguishable and showed a strong circulation. At cross-sectional station 9 ($x/L = 0.58$), shown in Fig. 24b, the two vortex cores are barely distinguishable and are observed as slightly darker regions on the picture. These visualization records show the lack of organized vortex motions over the aftbody. At station 10 ($x/L = 0.625$), Fig. 24c shows a region of stalled or separated flow and no clear sign of vortex cores or a pair of counter-rotating vortices. Furthermore, the oil-surface visualizations in Fig. 21 show that at similar flow conditions, the surface patterns consist of strong recirculation regions on both sides of the aftbody close to the left- and right-side meridians. The flow behaviors share many behaviors with vortex breakdown, but are also visibly different from the typical breakdown of strong leading-edge vortices.

IX. Longitudinal Stability of Finless DEX Projectile

The longitudinal stability, as indicated by the pitching-moment coefficient, of the two projectile models using the fin-A configuration was previously discussed and is shown in Fig. 6a. Results show that the e0.33-DEX is less stable than the hemi-DEX model for $\alpha > 30$ deg. Most of the nose-down pitching moment is expected to be generated by the horizontal fins.

An additional experiment was conducted to assess the longitudinal stability of both DEX models using a finless configuration in which no fins were incorporated to the projectile aftbody. Results from the pitching-moment coefficient of a finless DEX projectile are shown in Fig. 25. These results show, as expected, that both projectile models are longitudinally unstable (positive C_M) when the fins are removed. However, results show that for $\alpha \geq 46$ deg, the e0.33-DEX model shows a markedly larger nose-up pitching moment than shown with the hemi-DEX. The pitching-moment coefficient for the e0.33-DEX model is 27 and 96% higher at $\alpha = 46$ and 48 deg, respectively. Similarly, at $\alpha = 52$ deg, the pitching-moment coefficient is 138% higher for the e0.33-DEX than for the hemi-DEX model.

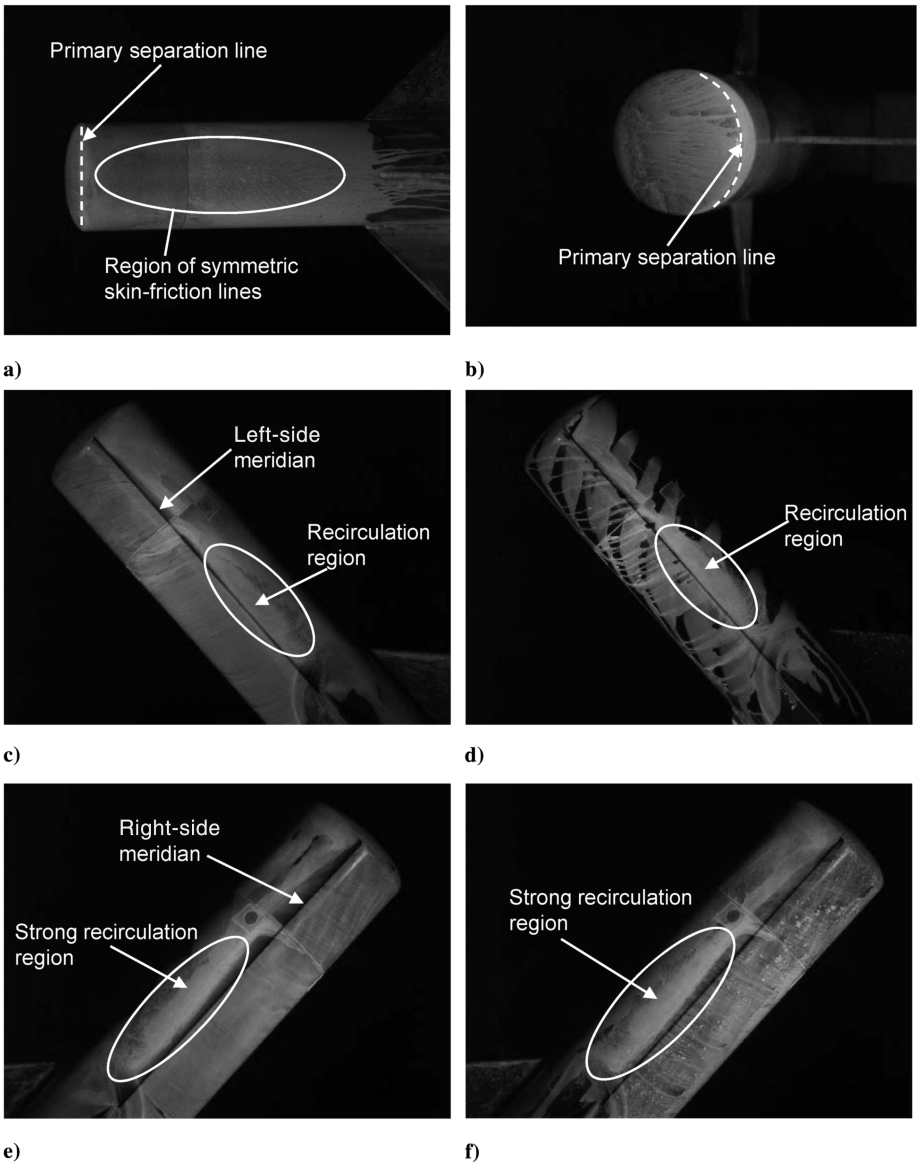

Fig. 21 Oil-surface visualizations for the e0.33-DEX model at $\alpha = 48$ deg, $\beta = 0$ deg, $U = 34$ m/s, and with the fin-A configuration: a) top view, b) left-side view, and c) right-side view.

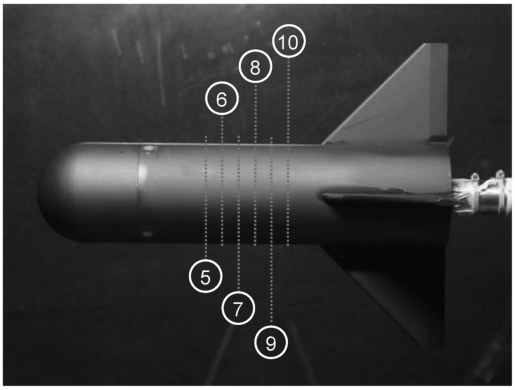

Fig. 22 Cross-sectional stations used for laser-sheet visualizations for vortex breakdown investigations; 5: $x/L = 0.42$, 6: $x/L = 0.46$, 7: $x/L = 0.5$, 8: $x/L = 0.54$, 9: $x/L = 0.58$, and 10: $x/L = 0.625$; the fin-A configuration was used.

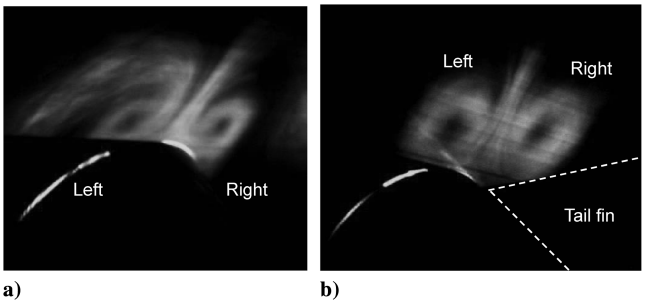

Fig. 23 Laser-sheet visualizations for the hemi-DEX model at $\alpha = 48$ deg, $\beta = 0$ deg, $U = 8.8$ m/s, and with the fin-A configuration: a) station 6 ($x/L = 0.46$) and b) station 10 ($x/L = 0.625$); pilot's point of view.

Pitching-moment coefficient results for the finless DEX configurations correlate well with the results obtained from vortex breakdown investigations. The study showed a lack of organized vortices over the aftbody of the e0.33-DEX model at $\alpha = 48$ deg. In contrast, no vortex breakdown was observed for the hemi-DEX model when two well-defined vortex cores were observed close to the tail fins. Vortex behaviors over the aftbody of the e0.33-DEX can help to explain the large difference in nose-up pitching moments for the finless DEX models for $\alpha \geq 46$ deg. Vortex breakdown over the aftbody of the e0.33-DEX model is expected to produce a reduction

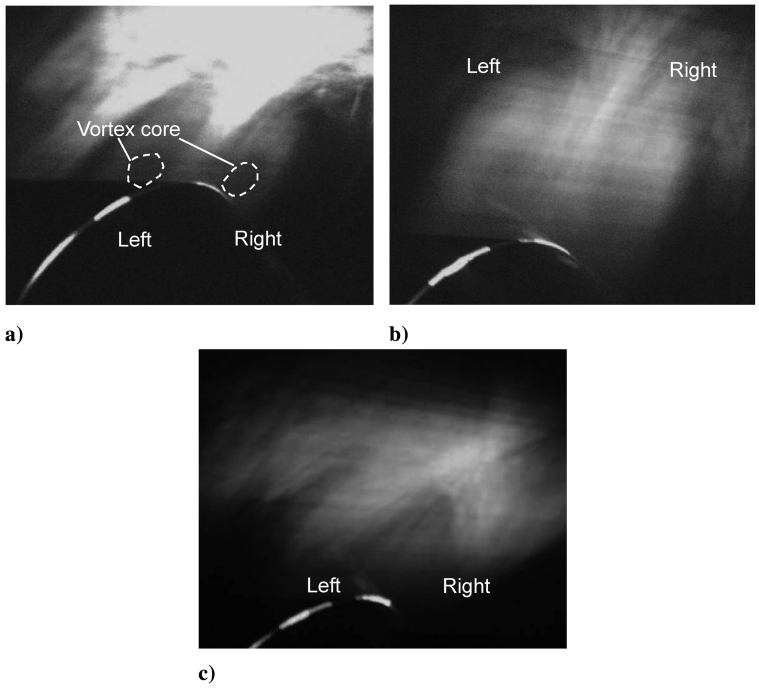

Fig. 24 Laser-sheet visualizations of the e0.33-DEX model at $\alpha = 48$ deg, $\beta = 0$ deg, $U = 8.8$ m/s, and with the fin-A configuration: a) cross-sectional station 5 ($x/L = 0.42$), b) station 9 ($x/L = 0.58$), and c) station 10 ($x/L = 0.625$); pilot's point of view.

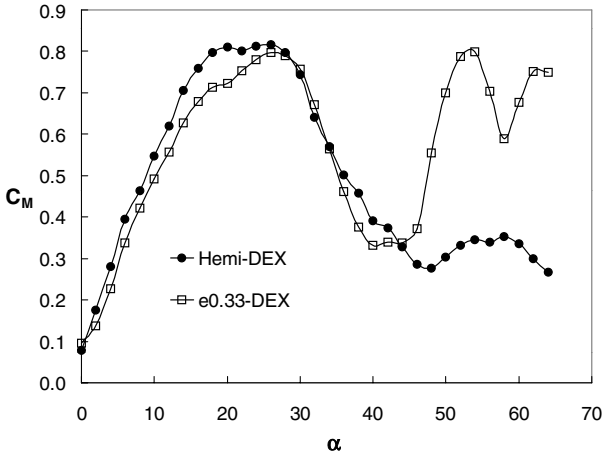

Fig. 25 Coefficient of pitching moment vs angle of attack for finless baseline DEX models at $M = 0.1$.

in the local lift, and the resultant normal force would be shifted forward toward the nose. This in turn would lead to an increase in the nose-up pitching moment, as observed in Figs. 6a and 25.

X. Source of Vortex Asymmetry

Side-force measurements clearly showed that the onset of vortex asymmetry for the hemi-DEX model is $\alpha = 36$ deg and for the e0.33-DEX is $\alpha = 56$ deg. As previously discussed, this shows that the hemi-DEX exhibits a behavior that is more akin to a pointed-nose body than to a blunt-nose body. Investigations on the effect of different fins on the side forces produced on both projectile models showed that there were almost negligible effects from the fins on the production of large side forces. These results indicate that the main contributor to earlier-than-expected onset of asymmetric forces on the hemi-DEX was the forebody geometry.

Both projectile models examined have rather blunt forebodies, and there is a large distance between the left- and right-side vortices. Hence, the source of vortex asymmetry is not expected to be due to vortex crowding at the tip of the nose, as was postulated by Keener and Chapman [52].

Based on results from detailed off- and on-surface visualizations presented earlier, Fig. 26 shows an interpretation of the flowfield pattern of the hemi-DEX model at high angles of attack ($\alpha \geq 40$ deg). One feature observed at both alpha conditions examined is the formation of a well-defined recirculation bubble in the front portion of the hemispherical forebody, but not in the elliptical forebody. Inside the separation bubble, the separation pattern indicates primary and smaller secondary forebody vortices with opposite senses of rotation. The hemispherical shape of the forebody results in a horseshoe vortex, as has been previously reported by others, including that over a hemisphere cylinder at high incidence by Wang et al. [56] based on water-tunnel visualizations. The strong kink in the separation line on the nose region indicates that the forebody vortex and aftbody flow begin to interact just downstream of the nose. Oil-surface visualizations did not show a break in the separation lines around this area, which suggests a merging of the forebody and aftbody vortices into a single vortex system. The forebody horseshoe vortex can potentially act as a communication link between the left-side and right-side aftbody vortices. This can lead to the formation of asymmetric vortices over the hemi-DEX aftbody, such as in the case of a pointed forebody in which the vortices are closely spaced at the nose.

Figure 27 shows an interpretation of the flowfield pattern of the e0.33-DEX model at high angles of attack, $\alpha \geq 40$ deg, based on results from detailed off- and on-surface visualizations. The e0.33-DEX showed the onset of vortex asymmetry at $\alpha = 56$ deg. Figure 27a shows that there are well-defined primary and secondary separation lines that are indicative of the presence of aftbody vortices. The aftbody vortices remain close to the leeward surface of the e0.33-DEX and do not lift off even at very high angles of attack as it occurs on the hemi-DEX. Further back on the aftbody, there is also a recirculation region with unsteadiness and it is indicative of a form of mild vortex breakdown. It is possible that these results indicate that the large side force observed above $\alpha = 55$ deg for the e0.33-DEX are due to an asymmetry in the location of vortex breakdown rather than asymmetric liftoff. Detailed surface pressure, not conducted during the present study, will provide a more definite answer.

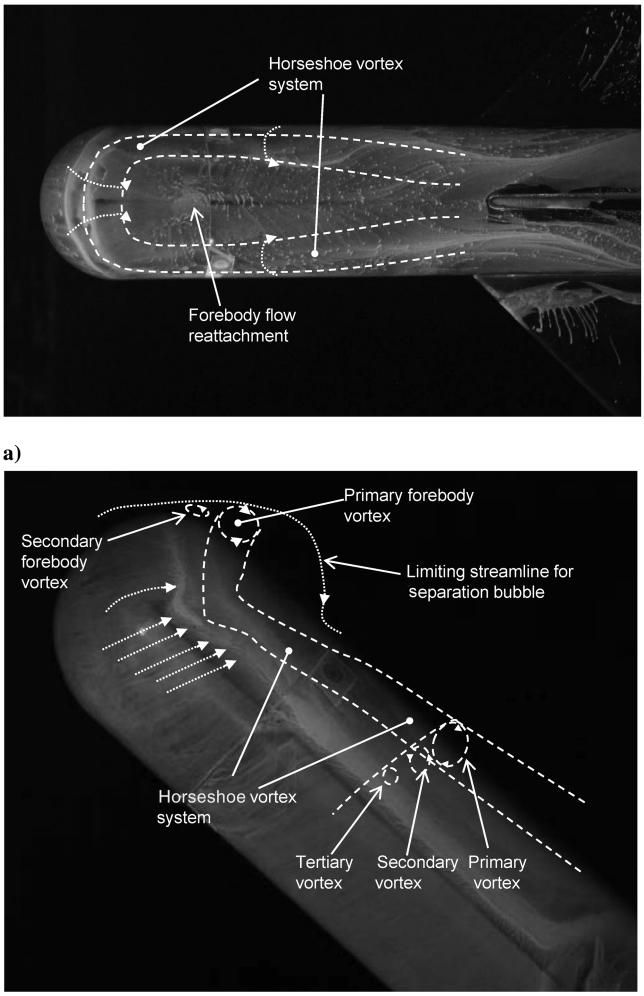

Fig. 26 Interpretation of the flowfield pattern for the hemi-DEX model based on off- and on-surface visualizations at $\alpha \geq 40$ deg, $\beta = 0$ deg, and $M = 0.1$: a) top view and b) side view.

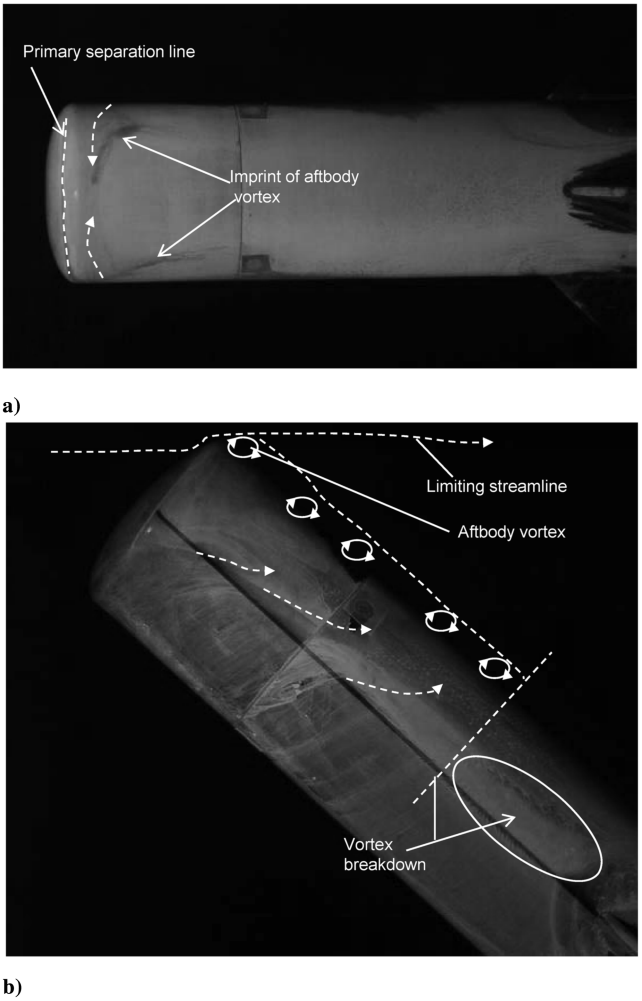

Fig. 27 Interpretation of the flowfield pattern for the e0.33-DEX model based on off- and on-surface visualizations at $\alpha \geq 40$ deg, $\beta = 0$ deg, and $M = 0.1$: a) top view and b) side view.

XI. Conclusions

A detailed investigation aimed at studying and understanding the flowfield around an e0.33-DEX (blunt elliptical forebody) and hemi-DEX (blunt hemispherical forebody) was conducted. The results show the dominant effect that the region close to the nose has on the development and evolution of the flowfield around short blunt-nose projectiles at high angles of attack. Some specific comments on results are the following:

1) The observed flow behaviors of the e0.33-DEX agree well with those expected for a blunt-nose slender body of revolution. In contrast, the development of flow asymmetry on the hemi-DEX exhibits characteristics of a pointed-nose body. As has been documented in the literature on other different forebody geometries [different elliptical ratio forebodies, pointed and ogive, and blunt forebodies (e.g., [18,19,24,30,35,44])], because the only difference between the two models is the nose geometry, the rather significant differences in flow behaviors can be attributed entirely to the difference in the nose flows.

2) Side-force measurements for the hemi-DEX model for three different fin configurations (A, B, and finless) showed that the large side forces and direction reversal of the forces were produced by the hemispherical forebody and there was very little contribution from the fins on the development of large out-of-plane forces. In addition, the angle of attack at which the maximum side forces were produced and reversed direction was within ± 2 deg for all three fin configurations examined. The magnitude and direction of the maximum side forces was almost identical for the hemi-DEX model with fin configurations A and B and showed a larger rightward-biased side force for the finless configuration.

3) The flow around the e0.33-DEX separates at the nose, with the aftbody vortices forming shortly downstream of the nose. The vortices are initially fairly wide apart due to the large stall region produced by the nose, but migrate quickly toward each other as the flow progresses downstream. The flow pattern results in the left and right vortices remain fairly symmetric until at very high angles of attack. It is possible that these results indicate that the large side force observed above $\alpha = 55$ deg for the e0.33-DEX are due to an asymmetry in the location of vortex breakdown rather than asymmetric liftoff. Detailed surface pressure, not conducted during the present study, will provide a more definite answer.

4) The flow around the hemi-DEX nose separates and reattaches to form a large recirculation bubble. A significant secondary flow also develops. The aftbody vortices form shortly downstream of the nose just as in the e0.33-DEX, but with the recirculation bubble over the hemi-DEX nose playing a more active role in the vortex-formation process. A horseshoe-vortex system forms over the forebody and extends to the aftbody. The horseshoe-vortex system can act as a communication link between the left and right vortices, thereby causing a flow behavior similar to that of a pointed nose. The initial trigger of vortex asymmetry can be microasymmetries in the nose, as suggested by some previous studies, or a hydrodynamic instability in the horseshoe-vortex system that is later transferred to the aftbody flow.

5) The vortex formed over a strake acts as an initiation point for the aftbody vortex. A sufficiently large strake can overcome the effect of

the nose and produce a similar control effect on either projectile configuration.

6) Detailed laser-sheet visualizations suggest that a mild form of vortex breakdown takes place on the aftbody region of the $e0.33$-DEX model at $\alpha = 48$ deg, with details of the process being unknown at present. In contrast, visualizations show two well-defined vortex pairs over the hemi-DEX aftbody at the same condition. The premise of vortex breakdown on the aftbody of the $e0.33$-DEX model is also supported by examining pitching-moment coefficient results for a finless DEX model. Results show that the $e0.33$-DEX model has a significantly larger nose-up pitching moment at $\alpha \geq 46$ deg than that of the hemi-DEX model. This decrease in longitudinal stability for the finless $e0.33$-DEX model correlates well with the observed aftbody vortex breakdown.

7) For the model roll orientation examined, the side forces produced on the $e0.33$-DEX model using an aftbody strake at optimized azimuthal and axial locations are generally about 50% lower than those produced on the hemi-DEX model under similar conditions, and the associated yawing moments are 20–50% lower on the $e0.33$-DEX than on the hemi-DEX model. These results, in part, support the assessment that vortices over the $e0.33$-DEX appear less organized visually than those over the hemispherical DEX, although no direct measurements (surface pressure or vorticity) were conducted.

Acknowledgments

This work was supported by Orbital Research, Inc., under Small Business Innovation Research (SBIR) Phase II contract no. FA8650-05-C-1834 issued by the U.S. Air Force Research Laboratory (AFRL). The authors would like to thank the U.S. Air Force Program Monitors Michael W. Pershing and William B. Blake for their encouragement and support of this work.

References

[1] Ericsson, L. E., and Reding, J. P., "Asymmetric Flow Separation and Vortex Shedding on Bodies of Revolution," *Tactical Missile Aerodynamics: General Topics*, Progress in Astronautics and Aeronautics, Vol. 141, AIAA, Washington, DC, 1991, pp. 391–452.

[2] Ericsson, L. E., and Reding, J. P., "Dynamics of Separated Flow over Blunt Bodies," NASA CR-76912, Dec. 1965.

[3] Hsieh, T., "Low Supersonic Flow over Hemisphere-Cylinder at Incidence," *Journal of Spacecraft and Rockets*, Vol. 14, No. 11, 1977, pp. 662–668.

[4] Hall, I. M., Rogers, E. W. E., and Davies, B. M., "Experiments with Inclined Blunt-Nosed Bodies at $M = 2.45$," Aeronautical Research Council, Research and Memoranda No. 3128, London, Aug. 1957.

[5] Dahlem, V., Flaherty, J., Sherida, D. E., and Przirembel, C. E. G., "High Angle of Attack Missile Aerodynamics at Mach Numbers 0.3 to 1.5," U.S. Air Force Wright Aeronautical Labs., Rept.TR-80-3070, Wright–Patterson AFB, OH, Nov. 1980.

[6] Dahlem, V., "Semi-Empirical Prediction Method for Induced Side Forces on Missiles at High Angles of Attack," AIAA, Paper 1979-25, Jan. 1979.

[7] Keener, E. R., Chapman, G. T., and Kruse, R. L., "Effects of Mach Number and Afterbody Length on Onset of Asymmetric Forces on Bodies at Zero Sideslip and High Angles of Attack," AIAA Paper 1976-66, Jan. 1976.

[8] Montividas, R., Reisenthel, P., and Nagib, H., "The Scaling and Control of Vortex Geometry Behind Pitching Cylinders," AIAA Paper 1989-1003, 1989.

[9] Patel, M. P., Sowle, Z. H., Stucke, R., and Ng, T. T., "Aerodynamic Control of a Small Projectile," AIAA Paper 2006-667, Jan. 2006.

[10] McKeehen, P. D., Pershing, M., Warner, D. A., and Blake, W. B., "Dynamic Modeling and Simulation of a Small Destructive Projectile," AIAA Paper 2001-4414, Aug. 2001.

[11] McKeehen, P. D., Pershing, Blake, W. B., and Warner, D. A., "Trajectory Analysis of Preliminary Designs for a Small Maneuvering Projectile," AIAA Paper 2003-5624, Aug. 2003.

[12] McKeehen, P. D., "GENESIS Simulation of a Modified VISTA/F-16," AIAA Paper 1995-3381, Aug. 1995.

[13] Cherry, M. C. et al., "A Systems Engineering Approach to Aircraft Kinetic Kill Countermeasure Technology: Development of an Active Air Defense System for the C/KC-135 Aircraft," M.S. Thesis, U.S. Air Force Inst. of Technology, Wright–Patterson AFB, OH, Dec. 1995.

[14] Cunningham, T., and Blake, W. B., "Wind Tunnel Study of a Fin Stabilized Guided projectile," AIAA Paper 2006-828, Jan. 2006.

[15] Lopera, J., Ng, T. T., Patel, M. P., and Vasudevan, S., "Yaw Control of a Blunt-Nose Projectile at High Angles of Attack Using Strakes," AIAA Paper 2007-0671, Jan. 2007.

[16] Allen, H. J., and Perkins, E. W., "Characteristics of Flow over Inclined Bodies of Revolution," NACA RM A50L07, 1951.

[17] Allen, H. J., and Perkins, E. W., "A Study of Viscosity on Flow over Slender Inclined Bodies of Revolution," NACA TN 1048, 1953.

[18] Peake, D. J., Rainbird, W. J., and Atraghji, E. G., "Three-Dimensional Flow Separations on Aircraft and Missiles," *AIAA Journal*, Vol. 10, No. 5, 1972, pp. 567–580.

[19] Lamont, P. J., and Hunt, B. L., "Pressure and Force Distributions on a Sharp-Debs-Nosed Circular Cylinder at Large Angles Of Inclination to a Uniform Subsonic Stream," *Journal of Fluid Mechanics*, Vol. 76, 1976, pp. 519–559. doi:10.1017/S0022112076000773

[20] Rao, D. M., "Side-Force Alleviation on Slender, Pointed Forebodies at High Angles of Attack," *Journal of Aircraft*, Vol. 16, No. 11, Nov. 1979, pp. 763–768.

[21] Ericsson, L. E., and Reding, J. P., "Alleviation of Vortex-Induced Asymmetric Loads," *Journal of Spacecraft and Rockets*, Vol. 17, No. 6, 1980, pp. 546–553.

[22] Ericsson, L. E., and Reding, J. P., "Steady and Unsteady Vortex-Induced Asymmetric Loads on Slender Vehicles," *Journal of Spacecraft and Rockets*, Vol. 18, No. 2, 1981, pp. 97–109.

[23] Ericsson, L. E., "Vortex Unsteadiness on Slender Bodies at High Incidence," *Journal of Spacecraft and Rockets*, Vol. 24, No. 4, 1987, pp. 319–326.

[24] Brandon, J. M., and Nguyen, L. T., "Experimental Study of Effects of Forebody Geometry on High Angle-of-Attack Stability," *Journal of Aircraft*, Vol. 25, No. 7, 1988, pp. 591–597.

[25] Ericsson, L. E., "Moving Wall Effects in Unsteady Flow," *Journal of Aircraft*, Vol. 25, No. 11, 1988, pp. 977–990.

[26] Ward, K., and Katz, J., "The Interaction Between primary and Secondary Flow Structures in the Lee of an Inclined Body of Revolution," AIAA Paper 1989-0143, Jan. 1989.

[27] Degani, D., and Schiff, L. B., "Numerical Simulation of the Effect of Spatial disturbances on Vortex Asymmetry," *AIAA Journal*, Vol. 29, No. 3, 1991, pp. 344–352.

[28] Degani, D., "Effect of Geometrical Disturbance on Vortex Asymmetry," *AIAA Journal*, Vol. 29, No. 4, 1991, pp. 560–566.

[29] Zilliac, G. G., Degani, D., and Tobak, M., "Asymmetric Vortices on a Slender Body of Revolution," *AIAA Journal*, Vol. 29, No. 5, 1991, pp. 667–675.

[30] Luo, S. C., Lim, T. T., Lua, K. B., Chia, H. T., Goh, E. K. R., and Ho, Q. W., "Flowfield Around Ogive/Elliptic-Tip Cylinder at High Angle of Attack," *AIAA Journal*, Vol. 36, No. 10, 1998, pp. 1778–1787.

[31] Lua, K. B., Luo, S. C., and Ho, E. K. R., "Helical-Groove and Circular-Trip Effects on Side Force," *Journal of Aircraft*, Vol. 37, No. 5, 2000, pp. 906–915.

[32] Hsieh, T., and Wang, K. C., "Three-dimensional Separated Flow Structure over a Cylinder with a Hemispherical Cap," *Journal of Fluid Mechanics*, Vol. 324, 1996, pp. 83–108. doi:10.1017/S0022112096007847

[33] Hoang, N. T., Rediniotis, O. K., and Telionis, D. P., "Symmetric and Asymmetric Separation Patterns Over a Hemisphere Cylinder at Low Reynolds Numbers and High Incidences," *Journal of Fluids and Structures*, Vol. 11, No. 7, Oct. 1997, pp. 793–817. doi:10.1006/jfls.1997.0106

[34] Hoang, N. T., Rediniotis, O. K., and Telionis, D. P., "Hemisphere Cylinder at Intermediate to High Reynolds Numbers," *AIAA Journal*, Vol. 37, No. 10, 1999, pp. 1240–1250.

[35] Kumar, R., Viswanath, P. R., and Ramesh, O. N., "Nose Bluntness for Side-Force Control on Circular cones at High Incidence," *Journal of Aircraft*, Vol. 42, No. 5, 2005, pp. 1133–1141.

[36] Fidler, J. E., "Active Control of Asymmetric Vortex Effects," *Journal of Aircraft*, Vol. 18, No. 4, 1981, pp. 267–272.

[37] Malcom, G., Ng, T. T., and Lewis, L., "Development of Non-Conventional Control Methods for High Angle of Attack Flight Using Vortex Manipulation," AIAA Paper 1989-2192, Aug. 1989.

[38] Ng, T. T., "Effect of a Single Strake on the Forebody Vortex Asymmetry," *Journal of Aircraft*, Vol. 27, No. 9, 1990, pp. 844–846.

[39] Stahl, W., "Suppression of Vortex Asymmetry Behind Circular Cones," *AIAA Journal*, Vol. 28, No. 6, 1990, pp. 1138–1140.

[40] Ng, T. T., and Malcom, G. N., "Aerodynamic Control Using Forebody Strakes," AIAA Paper 1991-0618, Jan. 1991.

[41] Ng, T. T., and Malcom, G. N., "Aerodynamic Control Using Forebody Blowing and Suction," AIAA Paper 1991-0619, Jan. 1991.
[42] Modi, V. J., Cheng, C. W., Mak, A., and Yokomizo, T., "Reduction of the Side Force on Pointed Forebodies Through Add-On Tip Devices," *AIAA Journal*, Vol. 30, No. 10, 1992, pp. 2462–2468.
[43] Chen, L., Ng, T. T., and Smith, B., "Forebody Vortex Control Using Nose-Boom Strakes," *Journal of Aircraft*, Vol. 32, No. 4, 1995, pp. 896–898.
[44] Viswanath, P. R., "Vortex Asymmetry and Induced Side Forces on Elliptic Cones at High Incidence," *Journal of Aircraft*, Vol. 32, No. 5, 1995, pp. 1018–1025.
[45] Hodgkin, H., and Wood, N. J., "Forebody Flow Control for Extended High-Angle-of-Attack Maneuvers," *Journal of Aircraft*, Vol. 35, No. 2, 1998, pp. 212–217.
[46] Patel, M. P., Tilmann, C. P., and Ng, T. T., "Closed-Loop Missile Yaw Control via Manipulation of Forebody Flow Asymmetries," *Journal of Spacecraft and Rockets*, Vol. 41, No. 3, 2004, pp. 436–443.
[47] Leu, T., Chang, J., and Lu, P., "Experimental Investigation of Side Force Control on Cone-Cylinder Slender Bodies with Flexible Micro Balloon Actuators," *Experimental Thermal and Fluid Science*, Vol. 29, No. 8, Sept. 2005, pp. 909–918. doi:10.1016/j.expthermflusci.2004.12.005
[48] Pick, G. S., "Investigations of Side Forces on Ogive-Cylinder Bodies at High Angles of Attack in the $M = 0.5$ to 1.1 Range," AIAA Paper 1971-570, Jun. 1971.
[49] Dexter, P. C., and Hunt, B. L., "The Effects of Roll Angle on the Flow over a Slender Body of Revolution at High Angle of Attack," AIAA Paper 1981-0358, Jan. 1981.
[50] Lamont, P. J., "Pressure Around an inclined Ogive Cylinder with Laminar, Transitional or Turbulent Separation," *AIAA Journal*, Vol. 20, No. 11, 1982, pp. 1492–1499.
[51] Yanta, W. J., and Wardlaw, A. B., Jr., "The Secondary Separation Region on a Body at High Angles of Attack," AIAA Paper 1982-0343, 1982.
[52] Keener, E. R., and Chapman, G. T., "Similarity in Vortex Asymmetries over Slender Bodies and Wings," *AIAA Journal*, Vol. 15, No. 9, 1977, pp. 1370–1372.
[53] Keener, E. R., and Chapman, G. T., "Onset of Aerodynamic Side Force at Zero Sideslip on Symmetric Forebodies at High Angles of Attack," AIAA Paper 1974-770, Aug. 1974.
[54] Fiechter, M., *Über Wirbelsysteme an Schlanken Rotationskörpern und Ihren Einfluss auf die Aerodynamischen Beiwerte*, Vol. 10/66, Deutsch-Französisches Forchungsinstitut, Saint Louis, France, Dec. 1966.
[55] Peake, D. J., Owen, F. K., and Higuchi, H., "Symmetrical and Asymmetrical Separations About a Yawed Cone," *High Angle of Attack Aerodynamics*, AGARD-CP-247, AGARD, Neuilly sur Seine, France, Jan. 1979, Paper 16.
[56] Wang, K. C., Hu, C. H., and Zhou, H. C., "The Separated Flow Structure over an Inclined Hemisphere-Cylinder," San Diego State Univ., Aerospace Engineering and Engineering Mechanics Rept. TR-89-02, San Diego, CA, 1984.